Article:
Doyle, Scott J., Shaw, David R., Kushner, Mark J. et al. (2026) Development of a Be reaction mechanism for plasma modelling. Plasma Physics and Controlled Fusion. 075037. ISSN: 1361-6587

https://doi.org/10.1088/1361-6587/ae88e8

Development of a Be reaction mechanism for plasma modelling

Plasma Physics and Controlled Fusion

OPEN ACCESS

RECEIVED
10 February 2026

REVISED
26 June 2026

ACCEPTED FOR PUBLICATION
9 July 2026

PUBLISHED
24 July 2026

PAPER

Development of a Be reaction mechanism for plasma modelling

Scott J Doyle[1,*], **David R Shaw**[2], **Mark J Kushner**[3] **and Erik Wagenaars**[2]

[1] Department of Physics, University of Aberdeen, School of Natural & Computing Sciences, King's College, Aberdeen AB24 3FX
[2] School of Physics, Engineering and Technology, University of York, York Plasma Institute, York YO10 5DD, United Kingdom
[3] Department of Electrical Engineering and Computer Science, University of Michigan, 1301 Beal Ave, Ann Arbor, MI 48109-2122, United States of America
[*] Author to whom any correspondence should be addressed.

E-mail: scott.doyle@abdn.ac.uk

Keywords: beryllium, redeposition, first wall, reaction mechanism, plasma-surface, etching

Abstract

Beryllium (Be), a soft alkaline earth metal, is used by the fusion community as a first wall material and within mixed-breeder blankets. During operation, Be is spread throughout the reactor and deposits on plasma-facing surfaces, including optical components. These Be coated surfaces readily oxidise forming BeO, degrading the optical properties and leading to Be and O being present in the plasmas formed near these surfaces. In this paper we present an $Ar/O_2/Be$ reaction mechanism for use in low-temperature plasma modelling, derived from calculated excitation, ionisation and momentum cross-sections for Be. Due to the similar properties of Be and aluminium (Al), Al is often used as a proxy in experiments; we compare plasma properties for Be containing plasmas with a well characterised $Ar/O_2/Al$ reaction mechanism. The two mechanisms produce similar plasma densities but dissimilar rates of diffusion, highlighting the limitations of using Al as a proxy. This work underlines that correct modelling of gas flow throughout the reactor is important in reliably predicting the re-deposition of eroded material such as BeO.

1. Introduction

Beryllium (Be) is a low-Z alkaline earth metal that is used in fusion reactors as a neutron multiplier within mixed breeder blankets [1], and as a first wall material in larger fusion experiments such as the Joint European Torus and smaller devices [2–4]. Its low atomic number is advantageous in plasma-facing applications where Bremsstrahlung losses are important. Be has a combination of nuclear, thermal, and mechanical properties that remain difficult to reproduce using substitute materials [5], including a high neutron multiplication capability, low density, and relatively high thermal conductivity. As a result, Be has been considered in several fusion-relevant contexts, including plasma-facing components, neutron breeder blanket concepts, x-ray diagnostic windows [6], and diagnostic or engineering components where low-Z, low-density materials are advantageous.

Although Be has been replaced by tungsten (W) in the ITER fusion device due to concerns around Be deposition on optical diagnostic mirrors [7–12], Be continues to be a material of significant importance to fusion-related applications. Sputtered Be and Be-containing reaction products can influence plasma-facing and diagnostic surfaces through erosion, redeposition, mixed-material layer formation, oxide formation, altered tritium retention, and dust or film generation [13–15]. These processes are relevant both to component lifetime and to the interpretation of data from, or degradation of, plasma-facing diagnostics. However, direct experimental investigation of Be-containing plasmas is limited primarily by the high toxicity, chemical reactivity, and associated costs of Be handling [16]. This has led to aluminium (Al) being used as a proxy in experimental studies [17]. Both elements readily form atmospheric oxides (BeO and Al_2O_3) which are electrical insulators and thermally stable. As a result, Be- and Al-containing plasmas, and plasma-facing surfaces containing BeO and Al_2O_3 are of interest to the fusion community.

There are limited experimental data available for beryllium metal sputtering yields via ion bombardment, and fewer for beryllium oxide. However it is known that in other gasses, such as deuterium, their threshold energies for sputtering (Be = 10 eV, BeO = 29 eV) are substantially lower than those for aluminium and aluminium oxide (Al = 36 eV, Al_2O_3 = 66 eV) [18], raising doubts about the suitability of Al as a universal proxy for Be sputtering, particularly where plasma–surface interactions are controlled by near-threshold ion bombardment. Numerical modelling provides a convenient way around the experimental limitations, allowing sputtering of Be itself and the validity of Al as a proxy for Be to be investigated under otherwise identical plasma conditions. For this modelling, a reaction mechanism for Be in the gas-phase plasma is needed, which is not currently available in a form suitable for plasma modelling and is therefore the focus of this paper.

In this paper we present a Ar/o2/Be gas-phase reaction mechanism (where Be is a sputtered product) for use in low-temperature and fusion-edge plasma modelling applications. Macroscopic properties of Ar/O_2/Be low-pressure (tens of mTorr) capacitively coupled plasmas employing this mechanism are compared to an otherwise identical Ar/O_2/Al plasma sustained within a Gaseous Electronics Cell (GEC) reactor geometry. Due to the sparse availability of experimental data for beryllium-containing plasmas, *ab-inito* computed electron impact cross-sections have been employed, including electron impact excitation [19–23], ionisation [23, 24], and momentum transfer [23]. The computed electron impact cross-sections utilised in this work, and the full raw data provided through personal communication with Zatsirinny, is presented within figures A1–A10 in the appendix.

2. Beryllium plasma chemistry

The new reaction mechanism employed in this work consists of elastic electron impact cross-sections for the first 19 excited states of Be; the excitation cross-sections from all of those states to all higher states (up to 4p 1P); super-elastic collisions from excited states to lower states, ionisation cross-sections for ground and the 2p 3P state; and momentum transfer for the ground state. To optimise for computational efficiency, some of the excited states that are close in energy have been lumped together. This is a common technique used in low-temperature plasma modelling and was previously used to create the Ar, O_2, and Al reaction mechanisms also used in this work [25–28]. In creating the lumped state, the cross-sections for each level are summed to create a cross-section for the lumped state with the threshold energy of the lumped state being the lowest threshold energy of the states. The statistical weight ($g = 2j+1$) of the lumped state is the sum of the statistical weights of the constituent states and the superelastic cross-section for the lumped state is that of the lowest contained excited state. The lumped Be states used in the reaction mechanism are shown in table 1. The statistical weights of each state were taken from Fuhr [29].

2.1. Ionisation and momentum transfer

Ionisation cross-sections for states BE3 and higher energy were obtained via the classical approach of Gryzinski [30–34],

$$\sigma = \pi a_0^2 \times N_{\mathrm{eq}} \times \left(\frac{E_{\mathrm{H,Thresh}}}{E_{\mathrm{Thresh}}}\right)^2 \times \frac{1}{U} \times \left(\frac{U-1}{U+1}\right)^{\frac{3}{2}} \times \left(1 + \frac{2}{3} \times \left(1 - \frac{1}{2U}\right) \times \log\left(2.7 + \sqrt{U-1}\right)\right). \quad (1)$$

In this equation, $U = E/E_{\mathrm{Thresh}}$ represents the incident electron energy (E) over the threshold energy of ionisation (E_{Thresh}); $E_{\mathrm{H,Thresh}}$ is the threshold ionisation energy of hydrogen; N_{eq} is the number of equivalent electrons in the outer shell and a_0 is the Bohr radius (0.529×10^{-10} m). As this approach is only being used for higher excited states, N_{eq} is set to 1. Threshold energies of ionisation for excited states are the differences between the ionisation energy for the ground state and the threshold energy of the excited state. Momentum transfer cross-sections were available for the ground state but not for any of the higher states. Assuming scattering is isotropic, elastic cross-sections for excited states were used as the momentum transfer cross-section.

2.2. Extrapolation to higher energies

Computed data for the cross-sections was available up to 110 eV and, as such, the higher energies must be accounted for through extrapolation of the data. It is known that dipole allowed transitions scale as $\log(E)/E$ and this is the slowest at which these cross-sections should decay with increasing energy

Table 1. Actual and lumped states addressing the first 19 excited states of Be for which cross-sections as available.

Lumped state	Threshold energy (eV)	Actual states
Be	0	Be(1 $s^2$2 s^2) ^{1}S
Be1	2.72	Be(1 $s^2$2s2p) ^{3}P
Be2	5.28	Be(1 $s^2$2s2p) ^{1}P
Be3	6.46	Be(1 $s^2$2s2p) ^{3}S, ^{1}S
Be4	7.05	Be(1 $s^2$2p^2) ^{1}D
Be5	7.3	Be(1 s^2s3p) ^{3}P, ^{1}P
Be6	7.4	Be(1 $s^2$2p^2) ^{3}P
Be7	7.69	Be(1 $s^2$2s3d) ^{3}D, ^{1}D; Be(1 $s^2$2s4d) ^{3}D, ^{1}D; Be(1 $s^2$2s4f) ^{3}F, ^{1}F
Be8	7.99	Be(1 $s^2$2s4s) ^{3}S, ^{1}S
Be9	8.28	Be(1 $s^2$2s4p) ^{3}P, ^{1}P

[35]. For transitions that become less dipole-like, the extrapolation of the cross-section to higher energies decreases more rapidly than for strictly dipole allowed transitions (e.g. $1/E^n$, $n \geqslant 1$). To extend the cross-sections to higher energies, the final 20% of the computed data were fitted via linear regression on a log–log plot, equivalent to a power-law extrapolation of the form $\sigma = E^a \exp(b)$, where a and b are fitted constants. This assumes that the cross-section decay is well established by approximately 80 eV. The fitted exponents ranged from approximately -0.3 to -3.3, with shallower decays corresponding to more dipole-allowed transitions and steeper decays to less dipole-like transitions, consistent with the expected physical behaviour [35].

2.3. Heavy particle interactions

Limited experimental or *ab-inito* computed data is available for Be heavy particle interactions [36, 37]. To address this, the heavy particle reactions considered in this Be mechanism were based upon existing Al reaction mechanisms. This decision is well precedented, as Al has often been used as an experimental proxy due to Be's high toxicity and chemical reactivity. Marot *et al* [17]. have shown the suitability of using Al as a proxy, as the similar electronegativity of both materials causes similar oxides and hydrides to form.

To estimate heavy particle reaction cross-sections with Be species, two models were employed. The first model employs the Langevin interaction cross-section σ_{L}, equation (2), which describes the classical interaction cross-section for ion–neutral interactions [38]. Charge transfer reactions including Be and/or Be^+ were computed using this cross-section,

$$\sigma_{\mathrm{L}} = \left(\frac{\pi \alpha_p q^2}{\epsilon_0 m_R}\right)^{1/2} \frac{1}{v_R} \tag{2}$$

where α_p is the polarisability of the neutral atom [39]; q is the elementary charge; m_R is the reduced mass of the atom and ion ($m_1 m_2 / m_1 + m_2$); and v_R is the relative velocity ($|v_1 - v_2|$). The reaction-specific rate coefficient was then computed as a function of the species state temperature via equation (3). Here, charge transfer reactions employ half the Langevin computed cross-section σ_{L},

$$K(T) = \int_0^\infty f_m v_R \sigma_{\mathrm{L}}(v_R)\, 4\pi v_R^2 \mathrm{d}v_R \tag{3}$$

and other symbols are as defined above. The temperature dependence is embedded by assuming a thermalised Maxwellian velocity distribution function, f_m, defined as,

$$f_m = \left(\frac{m_R}{2\pi kT}\right)^{3/2} \exp\left(-\frac{m_R v_R^2}{2kT}\right). \tag{4}$$

The charge transfer reaction rate ($K(T)$) was then fitted as a power function with respect to temperature, and the resulting exponential coefficient was taken as the input for the reaction rate in Arrhenius form, as shown in the Be/Ar/O_2 gas chemistry reactions in table 2.

A different interaction model was employed to compute Penning reaction rate coefficients, which were also included in the mechanism. Penning ionisation involves an interaction between an incident excited atom (A^*) and either a neutral atom (B) with an ionisation potential less than the excited state

Table 2. Argon, oxygen, and beryllium gas phase reactions and rate coefficients.

Species:
Ar, Ar^*, Ar^+, Ar_2^*, Ar_2^+, e^-
O_3, O_3^-, O_2, O_2^+, O_2^-, O, O^*, O^+, O^-,
Be, Be^+, Be^1 to Be9[a]

Reaction	Rate coefficient[b]	References[c]
$e + Be \leftrightarrow Be + e$	$f\epsilon$	[23]
$e + Be \leftrightarrow Be1 + e$	$f\epsilon$	[23]
$e + Be \leftrightarrow Be2 + e$	$f\epsilon$	[23]
$e + Be \leftrightarrow Be3 + e$	$f\epsilon$	[23]
$e + Be \leftrightarrow Be4 + e$	$f\epsilon$	[23]
$e + Be \leftrightarrow Be5 + e$	$f\epsilon$	[23]
$e + Be \leftrightarrow Be6 + e$	$f\epsilon$	[23]
$e + Be \leftrightarrow Be7 + e$	$f\epsilon$	[23]
$e + Be \leftrightarrow Be8 + e$	$f\epsilon$	[23]
$e + Be \leftrightarrow Be9 + e$	$f\epsilon$	[23]
$e + Be \rightarrow Be^+ + e + e$	$f\epsilon$	[23]
$e + Be1 \leftrightarrow Be1 + e$	$f\epsilon$	[23]
$e + Be1 \leftrightarrow Be2 + e$	$f\epsilon$	[23]
$e + Be1 \leftrightarrow Be3 + e$	$f\epsilon$	[23]
$e + Be1 \leftrightarrow Be4 + e$	$f\epsilon$	[23]
$e + Be1 \leftrightarrow Be5 + e$	$f\epsilon$	[23]
$e + Be1 \leftrightarrow Be6 + e$	$f\epsilon$	[23]
$e + Be1 \leftrightarrow Be7 + e$	$f\epsilon$	[23]
$e + Be1 \leftrightarrow Be8 + e$	$f\epsilon$	[23]
$e + Be1 \leftrightarrow Be9 + e$	$f\epsilon$	[23]
$e + Be1 \rightarrow Be^+ + e + e$	$f\epsilon$	[23]
$e + Be2 \leftrightarrow Be2 + e$	$f\epsilon$	[23]
$e + Be2 \leftrightarrow Be3 + e$	$f\epsilon$	[23]
$e + Be2 \leftrightarrow Be4 + e$	$f\epsilon$	[23]
$e + Be2 \leftrightarrow Be5 + e$	$f\epsilon$	[23]
$e + Be2 \leftrightarrow Be6 + e$	$f\epsilon$	[23]
$e + Be2 \leftrightarrow Be7 + e$	$f\epsilon$	[23]
$e + Be2 \leftrightarrow Be8 + e$	$f\epsilon$	[23]
$e + Be2 \leftrightarrow Be9 + e$	$f\epsilon$	[23]
$e + Be2 \rightarrow Be^+ + e + e$	$f\epsilon$	[23]
$e + Be3 \leftrightarrow Be3 + e$	$f\epsilon$	[23]
$e + Be3 \leftrightarrow Be4 + e$	$f\epsilon$	[23]
$e + Be3 \leftrightarrow Be5 + e$	$f\epsilon$	[23]
$e + Be3 \leftrightarrow Be6 + e$	$f\epsilon$	[23]
$e + Be3 \leftrightarrow Be7 + e$	$f\epsilon$	[23]
$e + Be3 \leftrightarrow Be8 + e$	$f\epsilon$	[23]
$e + Be3 \leftrightarrow Be9 + e$	$f\epsilon$	[23]
$e + Be3 \rightarrow Be^+ + e + e$	$f\epsilon$	[23]
$e + Be4 \leftrightarrow Be4 + e$	$f\epsilon$	[23]
$e + Be4 \leftrightarrow Be5 + e$	$f\epsilon$	[23]
$e + Be4 \leftrightarrow Be6 + e$	$f\epsilon$	[23]
$e + Be4 \leftrightarrow Be7 + e$	$f\epsilon$	[23]
$e + Be4 \leftrightarrow Be8 + e$	$f\epsilon$	[23]
$e + Be4 \leftrightarrow Be9 + e$	$f\epsilon$	[23]
$e + Be4 \rightarrow Be^+ + e + e$	$f\epsilon$	[23]
$e + Be5 \leftrightarrow Be5 + e$	$f\epsilon$	[23]
$e + Be5 \leftrightarrow Be6 + e$	$f\epsilon$	[23]
$e + Be5 \leftrightarrow Be7 + e$	$f\epsilon$	[23]
$e + Be5 \leftrightarrow Be8 + e$	$f\epsilon$	[23]
$e + Be5 \leftrightarrow Be9 + e$	$f\epsilon$	[23]
$e + Be5 \rightarrow Be^+ + e + e$	$f\epsilon$	[23]
$e + Be6 \leftrightarrow Be6 + e$	$f\epsilon$	[23]
$e + Be6 \leftrightarrow Be7 + e$	$f\epsilon$	[23]
$e + Be6 \leftrightarrow Be8 + e$	$f\epsilon$	[23]
$e + Be6 \leftrightarrow Be9 + e$	$f\epsilon$	[23]
$e + Be6 \rightarrow Be^+ + e + e$	$f\epsilon$	[23]

(Continued.)

Table 2. (Continued.)

$e + Be7 \leftrightarrow Be7 + e$	$f\epsilon$	[23]
$e + Be7 \leftrightarrow Be8 + e$	$f\epsilon$	[23]
$e + Be7 \leftrightarrow Be9 + e$	$f\epsilon$	[23]
$e + Be7 \rightarrow Be^+ + e + e$	$f\epsilon$	[23]
$e + Be8 \leftrightarrow Be8 + e$	$f\epsilon$	[23]
$e + Be8 \leftrightarrow Be9 + e$	$f\epsilon$	[23]
$e + Be8 \rightarrow Be^+ + e + e$	$f\epsilon$	[23]
$e + Be9 \leftrightarrow Be9 + e$	$f\epsilon$	[23]
$e + Be9 \rightarrow Be^+ + e + e$	$f\epsilon$	[23]
$Be1 \rightarrow Be$	$4.2 \times 10^{-1} s^{-1}$	[36]
$Be2 \rightarrow Be$	$5.52 \times 10^{8} s^{-1}$	[36]
$Be3 \rightarrow Be2$	$1 \times 10^{7} s^{-1}$	[36]
$Be3 \rightarrow B1$	$1 \times 10^{7} s^{-1}$	[36]
$Be4 \rightarrow Be2$	$1 \times 10^{5} s^{-1}$	[36]
$Be5 \rightarrow Be4$	$1 \times 10^{5} s^{-1}$	[36]
$Be5 \rightarrow Be3$	$1 \times 10^{7} s^{-1}$	[36]
$Be5 \rightarrow Be$	$1 \times 10^{6} s^{-1}$	[36]
$Be6 \rightarrow B1$	$1.41 \times 10^{8} s^{-1}$	[36]
$Be7 \rightarrow Be5$	$1 \times 10^{6} s^{-1}$	[36]
$Be7 \rightarrow Be2$	$2 \times 10^{7} s^{-1}$	[36]
$Be7 \rightarrow B1$	$5 \times 10^{7} s^{-1}$	[36]
$Be8 \rightarrow Be5$	$2 \times 10^{6} s^{-1}$	[36]
$Be8 \rightarrow Be2$	$5 \times 10^{6} s^{-1}$	[36]
$Be8 \rightarrow B1$	$2 \times 10^{6} s^{-1}$	[36]
$Be9 \rightarrow Be8$	$1 \times 10^{5} s^{-1}$	[36]
$Be9 \rightarrow Be7$	$1 \times 10^{6} s^{-1}$	[36]
$Be9 \rightarrow Be4$	$5.2 \times 10^{5} s^{-1}$	[36]
$Be9 \rightarrow Be3$	$2 \times 10^{5} s^{-1}$	[36]
$Be9 \rightarrow Be$	$1.2 \times 10^{5} s^{-1}$	[36]
$Be^* + Be \rightarrow Be + Be$	2.4×10^{-11}	[36, 38, 39][d]
$Be^* + Be \rightarrow Be + Be^*$	1.2×10^{-11}	[36, 38, 39][d]
$Be^+ + Be \rightarrow Be + Be^+$	1.2×10^{-11}	[36, 38, 39][d]
$Be^+ + Be1 \rightarrow Be + Be^+$	1.2×10^{-11}	[36, 38, 39][d]
$Be^+ + Be2 \rightarrow Be + Be^+$	1.2×10^{-11}	[36, 38, 39][d]
$Be^+ + Be3 \rightarrow Be + Be^+$	1.2×10^{-11}	[36, 38, 39][d]
$Be^+ + Be4 \rightarrow Be + Be^+$	1.2×10^{-11}	[36, 38, 39][d]
$Be^+ + Be5 \rightarrow Be + Be^+$	1.2×10^{-11}	[36, 38, 39][d]
$Be^+ + Be6 \rightarrow Be + Be^+$	1.2×10^{-11}	[36, 38, 39][d]
$Be^+ + Be7 \rightarrow Be + Be^+$	1.2×10^{-11}	[36, 38, 39][d]
$Be^+ + Be8 \rightarrow Be + Be^+$	1.2×10^{-11}	[36, 38, 39][d]
$Be^+ + Be9 \rightarrow Be + Be^+$	1.2×10^{-11}	[36, 38, 39][d]
$Be^+ + Ar \rightarrow Be + Ar^+$	$1.59 \times 10^{-11} \exp(-74698/T_g)$	[36, 38, 39][d]
$Be1 + Ar \rightarrow Ar^+ + Be + e$	$1.59 \times 10^{-11} \exp(-150858/T_g)$	[36, 38, 39][d]
$Be2 + Ar \rightarrow Ar^+ + Be + e$	$1.59 \times 10^{-11} \exp(-121847/T_g)$	[36, 38, 39][d]
$Be3 + Ar \rightarrow Ar^+ + Be + e$	$1.59 \times 10^{-11} \exp(-107922/T_g)$	[36, 38, 39][d]
$Be4 + Ar \rightarrow Ar^+ + Be + e$	$1.59 \times 10^{-11} \exp(-100959/T_g)$	[36, 38, 39][d]
$Be5 + Ar \rightarrow Ar^+ + Be + e$	$1.59 \times 10^{-11} \exp(-98638/T_g)$	[36, 38, 39][d]
$Be6 + Ar \rightarrow Ar^+ + Be + e$	$1.59 \times 10^{-11} \exp(-97478/T_g)$	[36, 38, 39][d]
$Be7 + Ar \rightarrow Ar^+ + Be + e$	$1.59 \times 10^{-11} \exp(-93996/T_g)$	[36, 38, 39][d]
$Be8 + Ar \rightarrow Ar^+ + Be + e$	$1.59 \times 10^{-11} \exp(-90515/T_g)$	[36, 38, 39][d]
$Be9 + Ar \rightarrow Ar^+ + Be + e$	$1.59 \times 10^{-11} \exp(-87033/T_g)$	[36, 38, 39][d]
$Be^+ + O \rightarrow Be + O^+$	$9.2 \times 10^{-12} \exp(-49847/T_g)$	[36, 38, 39][d]
$Ar^+ + Be \rightarrow Ar + Be^+$	1.2×10^{-11}	[36, 38, 39][d]
$Ar^+ + Be^* \rightarrow Ar + Be^+$	1.2×10^{-11}	[36, 38, 39][d]
$O^+ + Be \rightarrow O + Be^+$	1.2×10^{-11}	[36, 38, 39][d]
$O^+ + Be^* \rightarrow O + Be^+$	1.2×10^{-11}	[36, 38, 39][d]
$O_2^+ + Be \rightarrow O + O + Be^+$	9.17×10^{-12}	[36, 38, 39][d]
$O_2^+ + Be^* \rightarrow O + O + Be^+$	9.17×10^{-12}	[36, 38, 39][d]
$Ar_2^+ + Be \rightarrow Ar + Ar + Be^+$	4.58×10^{-11}	[36, 38, 39][d]
$Ar_2^+ + Be^* \rightarrow Ar + Ar + Be^+$	4.58×10^{-11}	[36, 38, 39][d]

(Continued.)

Table 2. (Continued.)

$Ar^* + Be \rightarrow Be^+ + Ar + e$	1.59×10^{-11}	[36, 38–40][ed]
$Ar_2^* + Be^* \rightarrow Be^+ + Ar + Ar + e$	2.75×10^{-12}	[36, 38–40][ed]
$Ar_2^* + Be \rightarrow Be^+ + Ar + Ar + e$	2.75×10^{-12}	[36, 38–40][ed]
$O^- + Be^+ \rightarrow O + Be$	1×10^{-7}	EST[ed]
$O_2^- + Be^+ \rightarrow O_2 + Be$	1×10^{-7}	EST[ed]
$O_3^- + Be^+ \rightarrow O_3 + Be$	1×10^{-7}	EST[ed]

[a] The lumped excited states of Be are detailed in table 1. Be* is representative of any excited state. Since the densities of Be and Al species are small, radiation trapping of transitions to the ground state have not been considered.

[b] Rate coefficients are in units of $cm^3 s^{-1}$ unless otherwise stated. $f\epsilon$ indicates that the rate coefficients have been calculated from the electron energy distribution within the eMCS. T_g is the gas temperature [K].

[c] References for the heavy particle reactions refer to the sources for the atomic properties used within the calculation for the Arrhenius coefficient and the threshold energy.

[d] Adjusted to gas temperature by $T_g^{0.5}$.

A^*, or another excited atom of the same species (A^{**}) where the combined excitation energy is greater than the ionisation potential of state A. In either case, the incident excited atom is quenched and the target atom is ionised, releasing an electron. The general form of the reaction is

$$A^* + B \rightarrow A + B^+ + e.$$

The Langevin interaction cross-section unfortunately cannot be used to determine Penning interaction cross-sections as it is only applicable for interactions between ions and neutral particles. Instead, the interaction cross-section for Penning processes, σ_P [Å^2], was calculated employing equation (5), formulated by Hotop and Niehaus [40],

$$\sigma_P = \pi R_0^2 \frac{n \exp^{-d\sqrt{E_i}}}{\sqrt{E_i} v r_B^2} 10^7. \quad (5)$$

This approach simply models the interaction as a *'billiard ball'* collision between two spherical potentials for species A^* and B. Here, R_0 is the combined radius of A and B ($r_A + r_B$) in Å, E_i is the ionisation potential of B in eV, v is the relative velocity in cm s^{-1}, n is the number of equivalent electrons in the outer shell of B, and d is the effective wall thickness if $R = R_0$ in Å. This effective wall thickness, d, is a measure of the potential barrier that an electron tunnels through from B to A. When compared with experiment, the value of d does not change regardless of the target atom. Therefore, d is largely determined by A, allowing it to be fixed and applied in the calculation of cross-sections for arbitrary target atoms. That being the case, Be has no Penning cross-section measurements and so the value of d cannot be obtained from comparison. For the purposes of this work the value for d has been set at 60% of R_0, which has been chosen through comparison of d for other species [41]. Once the Penning cross-sections were obtained from equation (5), the Penning ionisation rate reaction coefficients were then computed in the same fashion as the charge transfer reaction rate coefficients, using equations (3) and (4).

3. Numerical model and simulation geometry

In evaluating the Be mechanism we used the hybrid plasma equipment model (HPEM), which is a 2D modular simulator for low pressure plasmas. Detailed descriptions of the model can be found in [42–45] so only a brief description will be covered here. This investigation addresses a capacitively coupled plasma (CCP). The modules used are the electron energy transport module (EETM), which incorporates the electron Monte-Carlo simulation (eMCS), the fluid kinetics Poisson module (FKPM), and the plasma chemistry Monte-Carlo module (PCMC) for the computation of ion energy and angular distribution functions (IEADFs). Poisson's equation for electrostatic potential, and continuity, momentum and energy equations for heavy particles are computed in the FKPM. The electrostatic fields from the FKPM are used in the EETM in the eMCS. In CCPs, at the low pressures of interest (<75 mTorr), non-local electron heating is significant and electron transport cannot be dealt with using a fluid momentum equation [46, 47]. Instead, electrons are treated as pseudo-particles stochastically released from numeric cells in accordance with the electron density, with their paths integrated using the electrostatic fields from the

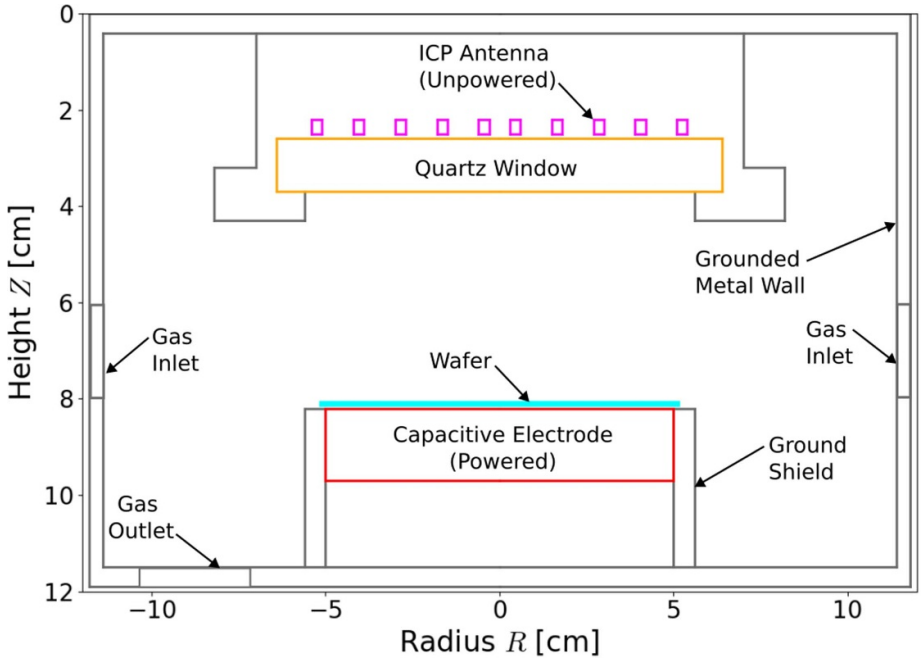

Figure 1. The Gaseous Electronics Cell (GEC) geometry employed in this work. The capacitive powered electrode is shown in red between $8 \leqslant Z \leqslant 10$ cm, the unpowered ICP antenna is shown in orange, the ICP window is shown in magenta, grounded walls are shown in grey, and the sputtered material wafer is shown in cyan.

FKPM in the eMCS. Spatially resolved collision frequencies are computed within each simulation cell employing the interacting species densities from the FKPM and relevant collision cross-sections. Within each time step, the pseudo-particle is advanced through a series of randomised events including [48] the collision probability and the collision type and scattering angle if the collision occurred. If no collision occurs, the pseudo-particle is advanced through another time step. The electron energy distribution function (EEDF) is constructed through statistically binning pseudo-particles in each simulation cell. Due to the computational expense of updating the pseudo-particle distributions, the EEDFs are updated once every 5 RF cycles (360 ns). The electron impact reaction rates and transport coefficients in each cell are computed from the EEDF, and are subsequently used in the FKPM along with other species densities and temperatures to compute reaction rates and update species and charge densities. The modules are iterated in this fashion until the cycle-averaged values for species densities converge.

All simulations presented in this work were performed in a GEC-like reactor geometry, shown in figure 1. This geometry was chosen as a relatively simple CCP geometry that enables future benchmarking of modelled results.

The simulated geometry consists of a 24 cm (0.2 cm/numerical cell) internal diameter by 12 cm (0.1 cm/cell) internal height cylindrically-symmetric aluminium vacuum chamber. All external walls are grounded aluminium, shown in grey. A 5.6 cm radius copper powered electrode (shown in red) is situated centrally, with a radial ground shield (shown in grey), on which a 0.2 cm thick dielectric wafer (shown in cyan) is placed. An axial gap of 4.2 cm separates the surface of the wafer from the quartz window above, behind which is a 5-turn inductively coupled plasma (ICP) antenna, which remains unpowered in this work, but does serve as an electrical ground. The wafer material properties were set to match the specific dielectric in each case, namely relative permittivity of $\epsilon_r = 7.0$ for beryllium oxide BeO and $\epsilon_r = 9.0$ for aluminium oxide (alumina) Al_2O_3. For both materials electrical conductivity was estimated at 1×10^{-16} S cm^{-1}.

The GEC reactor geometry employed in this work was originally configured as an ICP reactor with a DC table bias. As such, a coil antenna sits above the Quartz dielectric window (shown in orange). Here, for simplicity and ease of replication, the reactor was operated in a CCP mode, where the ICP antenna was unpowered. While the grounded ICP coils do not represent a conductive ground, due to the dielectric antenna window, they do still represent a ground for displacement current, and are fixed at 0 V. This is as distinct from the grounded vessel walls, which act as both a conductive and displacement ground at 0 V. Sputtering of Be, Al or O_x species occurred only from the wafer material on top of the powered electrode. For simplicity, no sputtering of the aluminium vessel walls, the copper powered electrode, or the Quartz dielectric windows was included.

Gas was introduced into the reactor from a radial inlet, positioned on the outboard wall between a height of 6 cm and 8 cm, and gas exited the reactor through an exhaust outlet positioned toroidally around the bottom of the chamber. argon gas was introduced at rate of 50 sccm, and the pressure at the outlet boundary was fixed at 8 mTorr, resulting in a pressure of 9 mTorr in the centre of the reactor.

An energy-independent ion-induced secondary electron emission coefficient of 0.2 was applied to the dielectric wafer on the powered electrode. Ions, accelerated to high energies through the powered electrode sheath, bombard the surface of the wafer resulting in sputtering and the release of secondary electrons. Secondary electrons are subsequently accelerated to non-thermal energies through the powered sheath and contribute approximately 10% of the total ionisation. Non-zero secondary electron emission from grounded surfaces produced a negligible change in the total ionisation, hence the secondary electron emission coefficient of all other materials was set to 0.0 for computational efficiency. Electron- and photon-induced secondary electrons were not considered in this study.

Ion-induced sputtering of Be and Al was modelled as an energy-independent process, with sputtered atom yields varying in direct proportion to the positive ion fluxes incident upon the wafer material. Incident positive ions (Ar^+, Ar_2^+, O^+, Al^+, and Be^+) quench with unity probability on the wafer surface, and were returned as their ground state species. In addition to returning the bombarding ion species, gas-phase Be and O, or Al and O, were returned with 0.20 probability for cases employing BeO and Al_2O_3 wafers, respectively. This sputtering yield was chosen as a conservative estimate between those identified in accelerator environments and real tokamak environments [49, 50]. Gas-phase excited Be and Al state fluxes quench with unity probability on all surfaces, returning as their ground state. Ground state Be and Al state fluxes stick with unity probability on all surfaces, and do not return to the gas phase.

4. Simulations of beryllium vs aluminium containing wafers

As a point of comparison, the new Be reaction mechanism was examined against a pre-existing Al reaction mechanism [12]. Here, three separate species of aluminium are modelled and tracked: Al refers to the Al(3 s^2 $2p^1$) ground state, Al1 refers to the Al(3 s^2 4 s^1) excited state ($\Delta E = 3.14$ eV), and Al2 is a lumped state containing: Al(3 s^2 $3p^2$), Al(3 s^2 3d), Al(3 s^2 4p), Al(3 s^2 5 s^1), Al(3 s^2 $4d^1$), Al(3 s^2 $5p^1$), Al(3 s^2 6 s^1), Al(3 s^2 $5d^1$), and Al(3 s^2 $6p^1$), see [12] for full details.

Two 'baseline' simulations were run employing the geometry shown in figure 1. The discharge conditions were identical in both cases, employing 9 mTorr of argon supplied at 50 sccm, and a 600 V_{pp} (peak-to-peak voltage), 13.56 MHz sinusoidal voltage waveform applied at the powered electrode. The material wafer was altered between simulations to introduce the different sputtered gas-phase components. Simulation 'A' employed an Al_2O_3 wafer and simulation 'B' employed a BeO wafer. In both cases there was a 20% probability of any cation impacting the wafer surface to sputter an Al, Be, or an O atom into the gas phase. In the case of an ion-induced sputtering event, the incident bombarding ion is also returned to the gas phase as a neutral, as is the case on all surfaces.

Macroscopic plasma properties, including the electron density, the argon ion density, the neutral argon density, and the electron temperature are shown in figures 2(a)–(d), respectively for a'baseline' discharge employing an Al_2O_3 wafer.

The macroscopic discharge properties were largely unaltered by the variation in wafer material and sputtered species. The Al and Be containing discharges exhibited only minor variations in electron density n_e and electron temperature T_e, both reaching maxima of $n_e = 3\times10^{16}$ m^{-3}, and $T_e = 4.1$ eV. In both cases the bulk time-averaged plasma potential was 34 V, and the wafer material accumulated a surface DC self-bias voltage of −155 V. This negative wafer bias arises to maintain equal charge in equal time towards both the larger grounded and smaller powered collecting areas, hence necessitating a higher flux towards the smaller powered area. A byproduct of this negative bias pulling a high flux of energetic cations towards a small area is a significant increase in the incident energy and hence a notable sputtering of the surface material. The rarefaction of the ground state Ar results from gas heating, where neutral gas temperature in the centre of the reactor is 370 K.

The relative invariance of the macroscopic properties arises due to the comparatively low sputtered ground-state Al and Be gas-phase densities (maximum densities of $\approx 1.5\times10^{16}$ m^{-3}) as compared to the background ground-state argon density (2.5×10^{20} m^{-3}), which primarily dictates the discharge dynamics. The maximum Ar^+ density in each case was 3.0×10^{16} m^{-3}, matching the electron density.

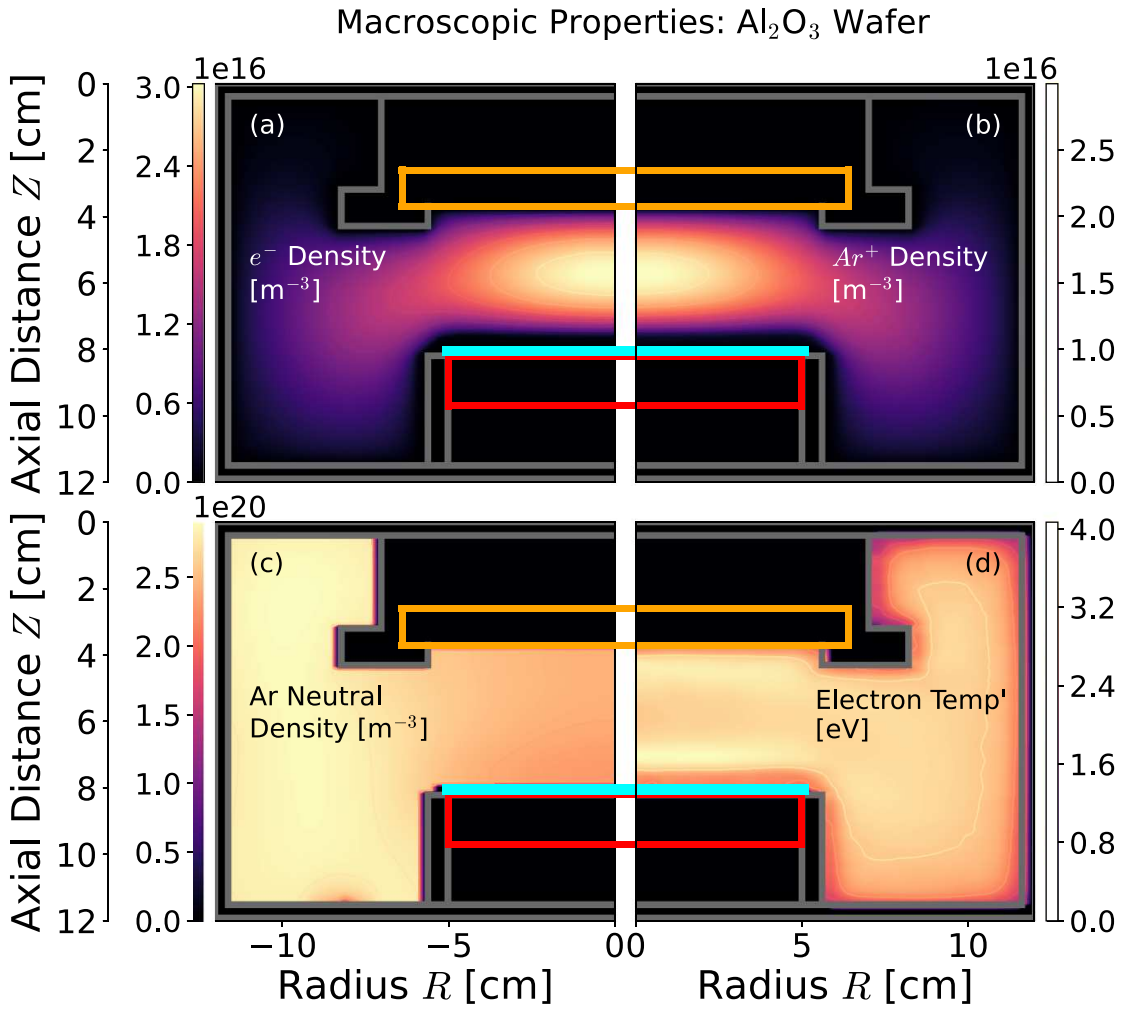

Figure 2. Representative macroscopic properties for a capacitively coupled discharge employing 600 V_{pp} at 13.56 MHz in 10 mTorr argon with an Al_2O_3 wafer. Subfigures contain the (a) the electron density, (b) the argon cation density, (c) the argon neutral density, and (d), the mean electron temperature. The scaling factor for the colour bar is noted at the top of each subfigure.

Sputtered metal cation densities are two-to-four orders of magnitude lower, with maximum densities of $n_{Al+} = 1.2\times10^{14}$ m^{-3} and $n_{Be+} = 3.5\times10^{12}$ m^{-3}, for the 'baseline' 600 V_{pp} cases.

The converged, reactor-averaged ionised and excited Be and Al species densities for the'baseline' simulations are shown in table 3. Here, as above, Al refers to the Al(3 s^2 $2p^1$) ground state. Al1 refers to the Al(3 s^2 4 s^1) excited state ($\Delta E = 3.14$ eV), and Al2 is a lumped state containing including open p, d, and s shells from Al(3s2 3p2) to Al(3s2 6p1).

The excited Be species in table 3 have densities that stratify into three distinct density'clusters', namely: (1) ground state Be and Be1 (2p and 3p); (2) the next populous state Be4 (1D2) and the Be^+ cation; followed by (3) the remaining excited Be states. We acknowledge that the reactor averaged densities of the higher excited states ($\geqslant$Be5) are small. These densities are retained in the table to emphasise the large dynamic range of excited state densities. We also note that with the higher excited states occupying a small fraction of the volume, these densities are perhaps artificially small due to the averaging. Returning to the lower excited states ($\leqslant$ Be4), the relative overpopulation of the Be4 state, as compared to Be2 and Be3, likely arises from preferential multi-step ionisation and excitation out of the Be2 and Be3 states, and is a result of the specific discharge conditions in this work. The energy gaps between the Be2 and Be3 states to the Be^+ cation are 4.04 eV and 2.86 eV, respectively; both of these are at-or-below the mean electron temperature of 4.1 eV, effectively depleting these metastable states. However, the energy gap from the Be1 state to the Be^+ cation is 6.6 eV, making Be2 the lowest state that is likely to undergo significant multi-step ionisation. Similarly, the mean electron temperature ($\approx$4 eV) closely aligns with the energy gap between Be1 to Be4 (4.33 eV), increasingly the probability of multi-step ionisation into the Be4 state from the populous Be1 state.

Table 3. Reactor averaged (avg') densities of (a) Al and (b) Be species in [m^{-3}]. Operating conditions: capacitive coupling employing 600 V_{pp} at 13.56 MHz, 10 mTorr argon.

Be species		Al species	
Species	Avg' density [m^{-3}]	Species	Avg' density [m^{-3}]
Be	5.06×10^{14}	Al	5.93×10^{14}
Be^+	2.74×10^{11}	Al^+	1.01×10^{13}
Be1	2.76×10^{13}	Al1	7.47×10^{11}
Be2	5.79×10^{8}	Al2	1.27×10^{14}
Be3	2.04×10^{9}	—	—
Be4	2.37×10^{11}	—	—
Be5	1.90×10^{9}	—	—
Be6	1.02×10^{8}	—	—
Be7	2.73×10^{8}	—	—
Be8	2.67×10^{8}	—	—
Be9	8.15×10^{8}	—	—

To further examine the differences between Al and Be containing discharges, the spatial density distributions of the 3 most populous excited Al and Be species, and their cations, have been plotted in figure 3. The operating conditions remain the same as previously discussed.

Sputtered ground-state Al and Be, shown in figures 3(a) and (b), have maximum densities adjacent to the wafer surface of 1.8×10^{16} m^{-3} and 1.2×10^{16} m^{-3}, respectively. The total inventories of each species also varies slightly, with 4.4×10^{12} sputtered Al atoms as compared to 3.7×10^{12} sputtered Be atoms. This slight discrepancy arises due to the small, but cumulatively significant,'self-sputtering' by wafer-incident Al^+ cations. As noted previously, the lower ionisation potential of Al leads to higher ion densities, see figures 3(c) and (d), and hence also higher wafer-incident fluxes. Here, the maximum wafer-incident Al^+ flux was 1.5×10^{17} m^{-2} s^{-1} as compared to a maximum Be^+ flux of 6.0×10^{15} m^{-2} s^{-1}. While Al^+ represents only ≈1% of the total wafer incident flux (Ar^+ flux is 2.5×10^{19} m^{-2} s^{-1}), this small enhancement compounds over time as more Al is sputtered, ionised, and accelerated back towards the wafer.

The topology of the most populous Al and Be states, shown in figures 3(e)–(h), exhibit notable differences in diffusion. Excited states Be1 and Al2 expand to fill the full region between the powered electrode and upper dielectric, while the lesser populated states, Be4 and Al1, are slightly more confined to the centre of the discharge. Specifically, Be4 and Al1 exhibit a rapid density gradient adjacent to the powered electrode, in the sheath region, while Be1 and Al2 are found to smoothly transition towards the wafer surface. As these states are not charged, their motion is not bound or dictated by the movement of the powered electrode sheath or applied RF voltage. The density drop-off must indicate either a rapid depletion of Be4 and Al1 within the sheath, or they must be preferentially created in the bulk.

To further examine this behaviour, 1D axial profiles of reactor-averaged ionised and excited Be and Al species densities for each simulation are shown in figures 4(a) and (b). Axial profiles are taken across the full height between the wafer and upper quartz dielectric window at a fixed radius of 1 cm. The locations of the powered electrode, wafer material, and quartz window are denoted in red, cyan, and yellow, respectively.

The densities of the spatially resolved ground state, excited, and ionised Be species in figure 4(a) exhibit the same general grouping as discussed above. As with the reactor averaged values, the densities of the higher excited states are small, due in part to the moderate power levels. We retain these densities to emphasise the large dynamic range of excited state densities. The ground state Be density is highest adjacent to the wafer surface, decreasing by a factor of 3 across the 4.2 cm gap towards the quartz window. Contrary to this trend, excited Be species exhibit reduced densities immediately adjacent to the wafer surface, in concordance with the Be^+ ion density. This reduction is most prominent for the low density states, averaging two orders of magnitude over the phase-averaged sheath extent (≈5 mm), and is less prominent for the more populous Be1 and Be4 states, decreasing less than one order of magnitude over the same distance. The axial profiles therefore reflect the distinction between surface-originating and volume-originating populations. Ground-state Be and Al are introduced at the wafer through ion-induced sputtering, so their densities remain strongly linked to the incident positive-ion flux and near-surface heavy-particle transport. The excited-state populations are produced mainly from these ground states through direct or multistep electron-impact excitation. As the sheath is depleted of electrons, these excitation pathways are suppressed near the wafer, causing the excited-state densities to reduce towards

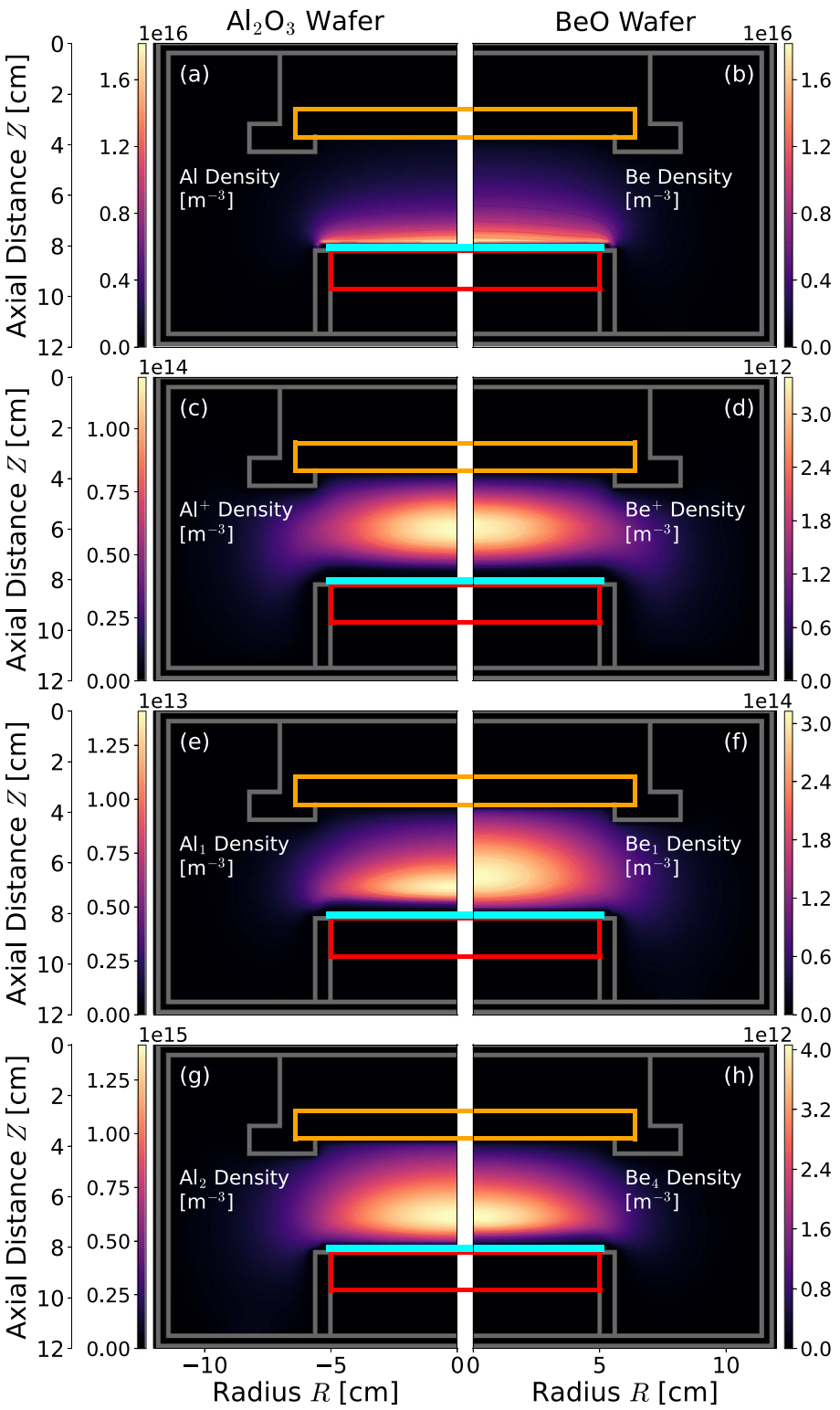

Figure 3. 2D density distributions of the most populous Be and Al states and their cations. Operating conditions: Capacitive coupling employing 600 V_{pp} at 13.56 MHz, 10 mTorr argon. Subfigures contain the (a) sputtered ground state Al density, (b) sputtered ground state Be density, (c) Al^{+} cation density, (d) Be^{+} cation density, (e) excited Al^{1} density, (f) excited Be^{1} density, (g) excited Al^{2} density, (h) excited Be^{4} density. The scaling factor for the colour bar is noted at the top of each subfigure.

the wafer surface. Excited states that persist further into the sheath (i.e. closer to the wafer) are therefore indicative of stronger coupling to heavy-particle dynamics, whereas states that collapse rapidly in the sheath are more strongly governed by electron-impact production.

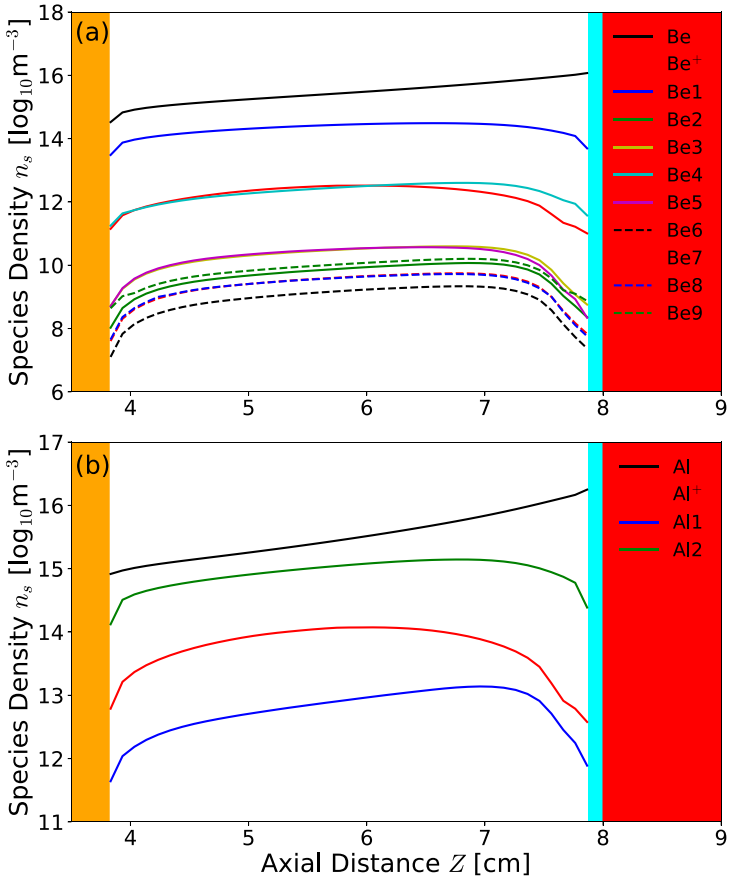

Figure 4. 1D Axial density profiles of all Be and Al states. Axial profiles are taken off-axis at a radius of $R = 1.0$ cm. The powered electrode is denoted in red, material wafer in cyan, and dielectric window in orange, for clarity. Operating conditions: capacitive coupling employing 600 V_{pp} at 13.56 MHz, 10 mTorr argon.

The same trends occur in the Al axial profiles, shown in figure 4(b). First, note the significantly steeper axial gradient in the ground state Al density. Secondly, a clear similarity in the spatial distribution of Al^+ and Al1 densities is observed, as compared to Al2, which is significantly flatter adjacent to the wafer surface. In both the Al and Be cases, the spatial distribution of the most populous metal excited states densities were the least 'coupled' to the ion density, i.e. were higher closer to the wafer surface. This indicates that these states likely arise more from direct electron impact excitation, and are less affected by heavy particle processes.

Of note, the species-specific ionisation fraction varies quite significantly for argon, aluminium and beryllium. Taking the argon cation density as a proxy for the total ion density, the reactor-averaged $^{Ar^+}/_{Ar}$ ionisation fraction for both cases is 3×10^{-5}. By comparison, the sputtered metal cations maintain higher species-specific ionisation fractions, with the reactor-averaged $^{Be^+}/_{Be}$ ion fraction of 5×10^{-4}, itself 30 times lower than the $^{Al^+}/_{Al}$ ion fraction of 1.5×10^{-2}. These values reflect the decreasing first ionisation potential from argon (15.76 eV), to beryllium (9.33 eV), to aluminium (5.98 eV), and is consistent with a Boltzmann-like heuristic scaling for single-step electron impact ionisation: $f_{ion} \approx \exp(-E_{IP}/T_e)$, where E_{IP} is the first ionisation potential. Computing this scale for the first ionisation potentials for Al and Be at a mean electron temperature of 4.1 eV gives a ratio of $^{f_{Al^+}}/_{f_{Be}} \approx 28$, which is in agreement with the numerically simulated value.

In Ar plasmas, ion–neutral charge exchange can be a primary production channel for sputtered metal ions whenever $k_{cx} n_{Ar+}$ (where k_{cx} is the ion–neutral charge exchange reaction rate coefficient) is comparable to, or exceeds, the effective electron-impact ionisation frequency. Consequently, metals undergoing substantial ion–neutral charge exchange reactions (e.g. Al and Be) will exhibit ion distributions that more closely follow the Ar^+ density in the plasma bulk. As the macroscopic properties, including Ar^+ density and distribution, are largely unaffected by wafer material in these cases, the rates of ion–neutral charge exchange will primarily differ in proportion to their rate coefficients. Here, the (Ar^+, Al) ion–neutral charge exchange reaction rate coefficient ($k_{cx} = 1.0 \times 10^{-9}$cm^{3}s^{-1}) is two orders of magnitude higher as compared to the (Ar^+, Be) coefficient ($k_{cx} = 1.2 \times 10^{-11}$cm^{3}s^{-1}), see table 2. This is

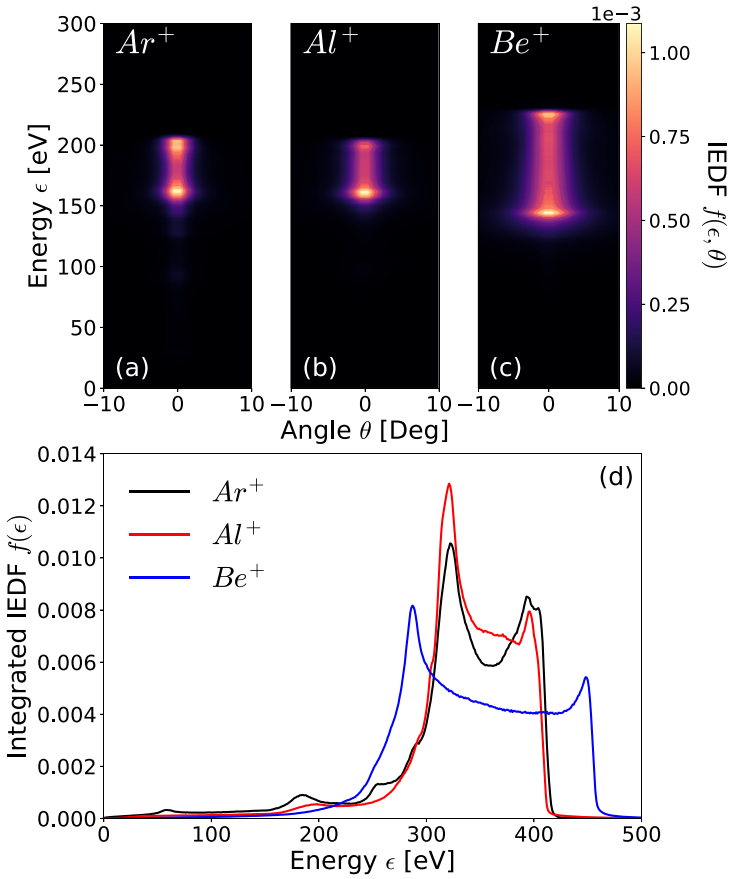

Figure 5. 1D ion energy and angular distribution functions (IEADFs) incident upon the wafer surface at $R = 2.5$ cm. IEADFS were captured with an energy resolution of 0.5 eV and an angular resolution of 0.5 degrees. Conditions: capacitive coupling employing 600 V_{pp} at 13.56 MHz, 10 mTorr argon. The scaling factor for the colour bar is noted at the top of each subfigure.

qualitatively consistent with the density distributions presented in figures 3 and 4 where Al^+ and Be^+ are bulk-localised, while ground-state Al and Be are surface-localised, indicative of a volumetric ion-creation pathway such as charge exchange. The individual contributions from each ion–neutral charge exchange pathway are not treated explicitly here.

As noted previously, sputtered metal ions in the bulk may be accelerated back towards the wafer where they will either participate in further sputtering, or may redeposit on the wafer surface. Differences between Al and Be ions incident upon the wafer surface was briefly investigated, where the Ar^+, Al^+, and Be^+ IEADF incident upon the wafer surface at $R = 2.5$ cm are shown in figure 5(a)–(c). These IEADFs were obtained from the two 'baseline' case simulations employing the PCMC model [42]. Angle-integrated IEADF are presented in figure 5(d) for ease of comparison. The Ar^+ IEADF is presented for the BeO wafer'baseline' case, there were no significant differences in the Ar^+ distribution from either case.

Here, all IEADFs exhibit a bimodal energy distribution with a narrow angular spread, typical of low-pressure radio-frequency sheaths, where the ion sheath transit timescale τ_{ion} is shorter than the RF period: $\tau_{ion} << 1/\nu_{RF}$. Both Ar^+ and Al^+ exhibit a bi-modal distribution with a major peak at 310 eV and 390 eV, while the Be^+ exhibits a broader and slightly up-modulated distribution with peaks at 280 eV and 450 eV. This distribution is as expected, and arises from two related considerations. Firstly, lighter Be^+ ions are accelerated more rapidly, resulting in a more instantaneous response to the applied RF field and the observed broader extrema in energy. Secondly, the faster moving and smaller cross-section Be^+ ions have a lower collisional probability, leading to sharp, well-defined energy peaks. The former of these points is a purely mass-based consideration, but the latter results from particular choices regarding the inclusion of ion–neutral charge–exchange reactions, and their cross-sections, for each ion and neutral species.

To assess the robustness and utility of the Be reaction mechanism beyond the 'baseline' 600 V_{pp}, 10 mTorr case, two additional parameter scans were performed in which the neutral pressure and applied RF voltage were varied independently. The Be ground state density for the extrema in pressures

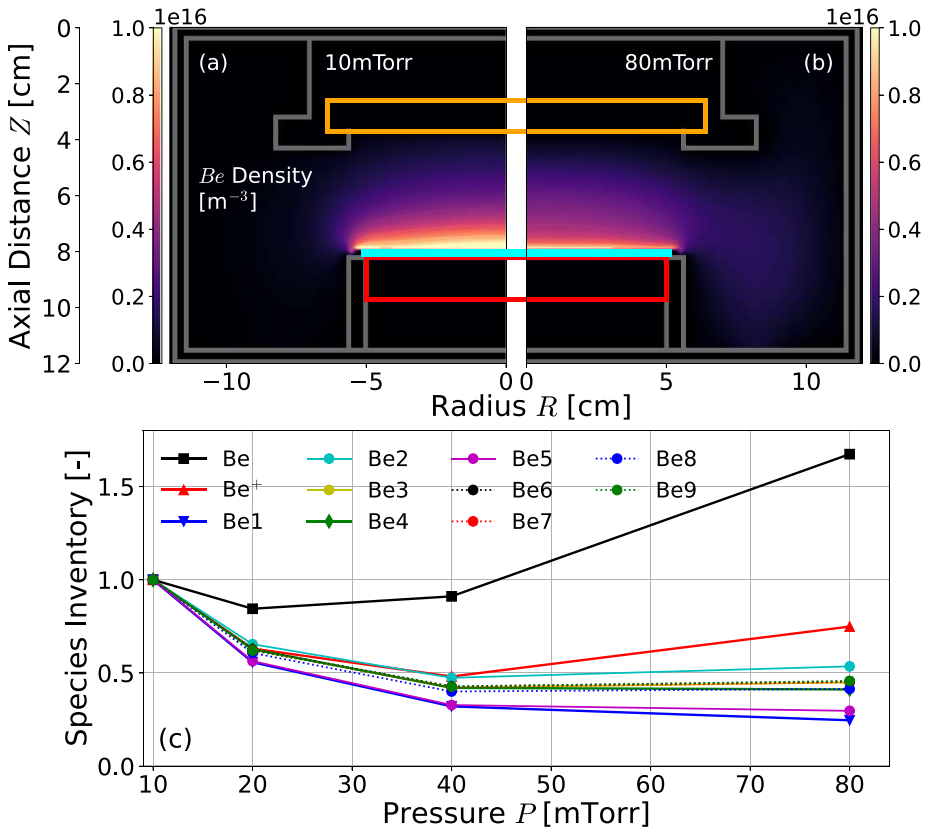

Figure 6. 2D Be ground state densities for operation at (a) 10 mTorr and (b) 80 mTorr, and (c) 1D profiles of reactor integrated Be species densities for varying pressure. Operating conditions: capacitive coupling employing 600 V_{pp} at 13.56 MHz, 10–80 mTorr argon. The scaling factor for the colour bar is noted at the top of each subfigure.

(10 mTorr and 80 mTorr) are shown in figures 6(a) and (b), while the excited-state inventories with respect to increasing neutral gas pressure, from 10 mTorr to 80 mTorr, are shown in figure 6(c). All cases were performed under otherwise identical operating conditions to the'baseline' case, noting that while the voltage was maintained at a constant value, total power deposited was allowed to vary, from 9.2 W at 10 mTorr to 7.1 W at 80 mTorr.

Increasing the pressure from 10 to 80 mTorr reduces the maximum Be density adjacent to the wafer by approximately 33%, see figures 6(a) and (b). In contrast, the integrated Be species inventory, i.e. the total absolute number of a species within the simulation domain, increases by approximately 60% over the same pressure range, see the solid black line in figure 6(c). A decrease in maximum density coinciding with an increase in inventory indicates that higher pressures suppress local accumulation while increasing overall retention of Be. This increase in neutral density is not associated with enhanced sputtering of Be, as the dominant Ar^+ ion flux to the wafer actually slightly decreases from 2.5×10^{19} m^{-2} s^{-1} at 10 mTorr to 1.7×10^{19} m^{-2} s^{-1} at 80 mTorr. Instead, the increase in Be inventory simply reflects a shift from a less-collisional regime at low pressures to a more-collisional, diffusion-limited, regime at high pressures. Assuming a near-constant sputtered Be flux, Γ_{Be}, the diffusion term, D_{Be}, will be density-gradient limited, where: $\Gamma_{Be} = D_{Be}\nabla n_{Be} = constant$. All else being equal, the shallower wafer-adjacent Be density gradient exhibited in figure 6(a) enforces a higher diffusivity at the location of highest density. Conversely, the steeper wafer-adjacent density gradient in figure 6(b) enforces a lower diffusivity, and hence a slower transport of Be to the walls, which represents the main loss mechanism in this work. A more-collisional lower diffusivity discharge, therefore, maintains a higher time-averaged reactor Be inventory, as observed.

The above reasoning also agrees with the observed suppression of all excited states with increasing pressure. The reduction in excited-state inventories arises due partly to enhanced collisional relaxation pathways with neutral argon, of form $Be_x + Ar \Rightarrow Be_{ground} + Ar$, and partly due to enhanced Penning ionisation pathways, of form $Be_{excited} + Be_{excited} \Rightarrow Be^+ + Be_{ground}$, as metastable species collide more frequently with each other. Enhanced Penning processes contribute to the observed increase in the Be^+ ion inventory from 10 to 80 mTorr, see solid red line with triangle markers in figure 6(c), despite a

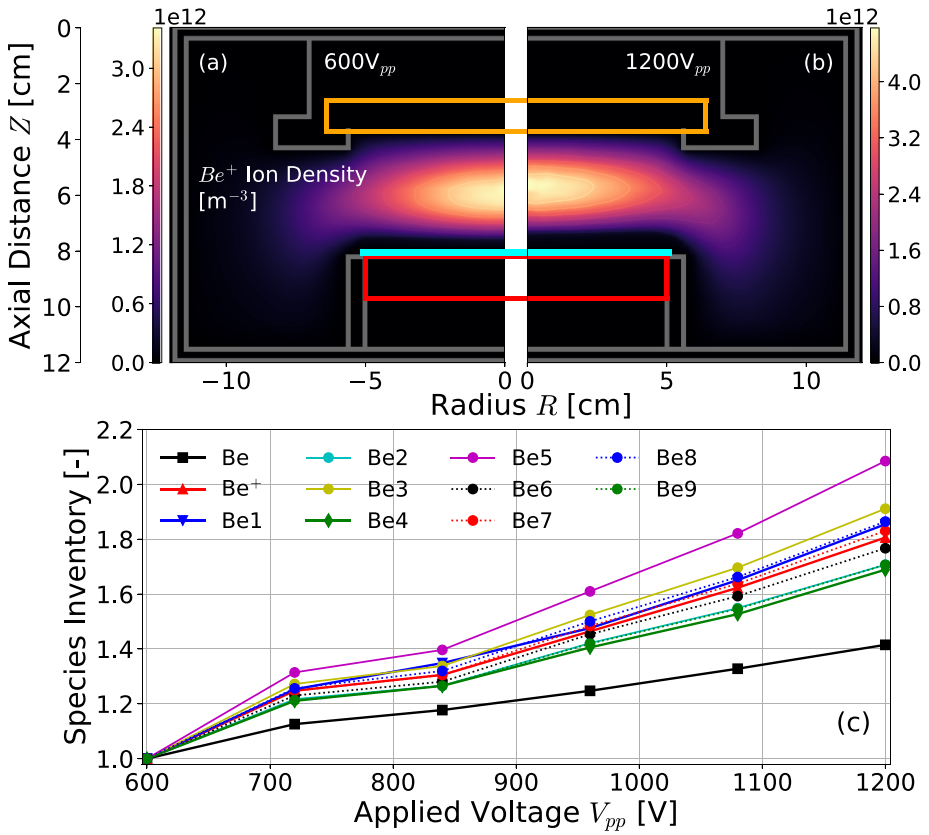

Figure 7. 2D Be^+ cation state densities for operation at (a) 600 V_{pp} and (b) 1200 V_{pp}, and (c) 1D profiles of reactor integrated Be species densities for varying applied voltage. Operating conditions: Capacitive coupling employing 600 V_{pp}–1200 V_{pp} at 13.56 MHz, 10 mTorr argon. The scaling factor for the colour bar is noted at the top of each subfigure.

7% reduction in the deposited RF power between these two pressures. Higher pressures therefore more efficiently produce sputtered metal ions and more readily retain sputtered metal neutrals.

A complementary voltage scan was also performed, where the Be^+ ion density is presented for the extrema in tested voltages in figures 7(a) and (b), and the total reactor inventory of all excited species is presented in 7(c) with respect to varying applied voltage. Power was again allowed to vary, increasing from 9.2 W at 600 V_{pp} to 25.1 W at 1200 V_{pp}.

Increasing the applied voltage increases key macroscopic properties. The electron and Ar^+ densities rise by 20% over the voltage range scanned, reaching a maximum of 3.6×10^{16} m^{-3}. In contrast, the Be^+ density responds more strongly, increasing by $\approx 50\%$ from 3.1×10^{12} m^{-3} to 4.6×10^{12} m^{-3}, exhibiting greater sensitivity to the increased voltage due to the aforementioned $\exp(-E_{IP}/T_e)$ scaling. Here, the sheath-localised electron temperature increases from 4.1 eV at 600 V_{pp} to 5.7 eV at 1200 V_{pp}, increasing the proportion of direct electron impact ionisations expected within the sheath. The phase-averaged powered-electrode sheath also expands with increasing voltage, following $X_s \propto \sqrt{\frac{2V_s\epsilon_0}{en_{Ar^+}}}$. Over the voltage scan, the sheath voltage V_s increases by 220% (from -184 V to -409 V), driven primarily by an increasing DC self-bias voltage, resulting in a net sheath thickening. Despite this change in charged species discharge topology, the spatial distributions of ground and excited Be neutrals remain broadly similar for all applied voltages.

The wafer-incident Ar^+ ion flux increases proportionally with applied voltage, rising by 20% to 3.1×10^{19} m^{-2} s^{-1} at 1200 V_{pp}, matching the change in Ar^+ ion density. Maximum ion energies also increase, producing a high-energy-weighted bi-modal IEDF in the range 350–440 eV at the wafer surface. Since the present model assumes an energy-independent sputter yield for all incident ions ($Y = 0.2$), the Be source term is likely underestimated at higher voltages. Despite this, a near-monatomic increase in the total Be inventory is observed for all charge and excitation states, see figure 7. Ground-state Be increases least strongly, while the higher-lying lumped excited states (Be5–Be9) show the largest relative growth, consistent with the higher T_e and a greater collisional probability within the wider sheath region at larger applied voltages. These results indicate that, even with a fixed sputter yield, the Be inventory remains strongly voltage-dependent due to coupled changes in ionisation efficiency, sheath extent,

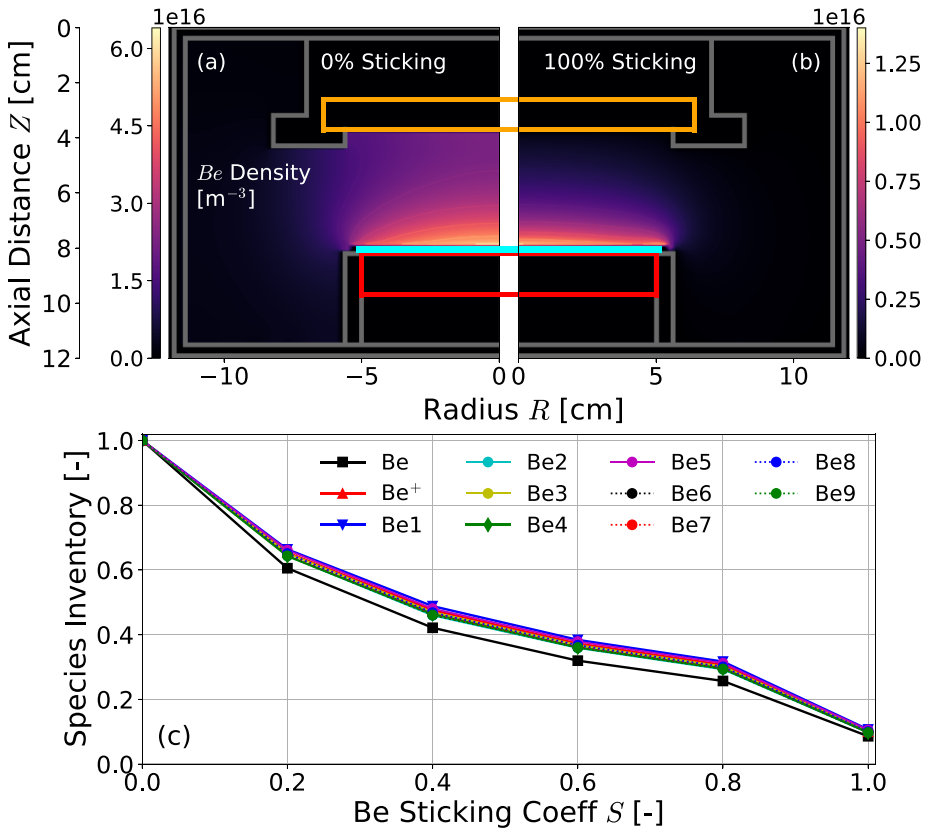

Figure 8. 2D Be ground state densities for (a) zero probability (always stick) and (b) unity probability (always stick) of wall loss. Sub-figure (c) shows 1D profiles of reactor integrated Be species densities for varying sticking coefficient. Operating conditions: Capacitive coupling employing 600 V_{pp}–1200 V_{pp} at 13.56 MHz, 10 mTorr argon. The scaling factor for the colour bar is noted at the top of each subfigure.

and electron temperature, suggesting that the voltage scaling of Be sputtering and transport cannot be inferred from the dominant ion behaviour alone.

To assess the effects of wall losses on the spatial distribution and relative abundance of Be a scan of the Be sticking coefficient was performed for the same baseline conditions as in figure 3(a). To make this scan tractable, only the sticking coefficient for ground state Be was altered. Other species sticking and return coefficients remain unchanged, where all excited states of Be have unity probability to stick and return as ground state Be.

Altering the Be sticking coefficient was found to have a significant effect on both the topological distribution of Be and species inventories. The topological distribution for zero wall sticking of Be is shown in figure 8(a), and broadly fills the volume between the wafer and upper quartz window. In contrast, the topology for a unity sticking coefficient, shown in figure 8(b) exhibits a much steeper gradient in Be density falling off from the wafer surface. It should be again stated that all prior cases in this work employed a unity sticking coefficient, as shown in (b). The sticking coefficient for ground state Be appears to set the trend for all lumped excited states assessed in this study, where all lumped species inventories shown in figure 8(c) change in lock-step with the ground state density. This close coupling between the Be ground state and excited state densities arises due to the broad range of radiative transitions, collisional relaxation, and excitation transfer reactions included in the model. The maximum variation in species inventory is exhibited by the Be ground state, which is to be expected, which increases by a factor of 20 over the sticking coefficient range 1–0. The same parameters are shown for the variation of the sputtering yield in figure B1, where the species inventories increase nearly linearly, varying by a factor of 15 for an increase in sputtering yield by a factor of 16. No significant alteration in topology was observed for variations in sputtering yield. The significant variation in both topology and inventory with respect to sticking coefficient, as compared to yield, identifies wall loss processes as the more important surface coefficient to understand for reliable application of this model to a specific geometry or discharge.

5. Conclusions

A Be/O/Ar reaction mechanism was developed for use in modelling low-temperature fusion-edge plasmas. Simulations performed in a Gaseous Electronics Reactor (GEC) showed similarities in discharge behaviour to Al metal containing plasmas. Macroscopic discharge conditions, such as electron density, temperature, and plasma potential were largely unaffected by the introduction of Be, as compared to Al. However, dissimilarities in diffusivity and ion fractions were observed, which could lead to significant behavioural differences in practice, for instance altering neutral impurity flow streams and the extent to which the background magnetic topology must be taken into account (e.g. for impurities with high ion fractions).

The findings underscore that Be production and redeposition rates in fusion cleaning plasmas depend not only on the dominant ion flux to the surface but also on sheath-driven changes in electron temperature and ion/neutral diffusivity and residence time. Relatively small changes in background pressure (10's of mTorr) were found to notably alter the Be inventory, suppressing metastable formation and enhancing multi-body and Penning ionisation processes, leading to enhanced neutral and singly ionised Be inventories within the bulk. This implies that at higher neutral pressures, such as those within regions of neutral gas puffing, metallic ion redeposition on first mirrors may be less localised than currently assumed. For situations where the production of sputtered metal ions is of benefit, this work predicts that a careful consideration of the pressure regime is critical to maximising the'utility' of excited state ladder climbing and achieving efficient ion generation.

This work highlights the current limitations in our understanding of BeO and other metal oxide erosion processes, and underpins the need for further experimentation. Although experimental studies have been conducted, they have largely been restricted to a small range of geometries and parameter regimes [51]. More generally, we show that the commonly performed comparisons with Al_2O_3 to estimate other metal oxide etching rates can be insufficient, a conclusion backed by results in different gasses showing a significant difference in the threshold energies for sputtering [18]. With a better understanding of BeO and Al_2O_3 surface etching through experimental testing, and validation of the developed mechanism, etching rates and profiles could be predicted in future fusion devices.

Acknowledgments

This work was supported by the Engineering and Physical Sciences Research Council (EPSRC) [EP/L01663X/1 & EP/K018388/1].

Data availability statement

All data that support the findings of this study are included within the article (and any supplementary files).

Data access

All data created during this research are available by request from the University of Aberdeen or the University of York's Research Databases.

Author contributions

Scott J Doyle 0000-0002-8741-1018
Conceptualization (supporting), Data curation (lead), Formal analysis (lead), Investigation (equal), Methodology (equal), Software (lead), Validation (lead), Visualization (lead), Writing – original draft (equal), Writing – review & editing (equal)

David R Shaw 0000-0001-5542-0334
Conceptualization (equal), Data curation (equal), Formal analysis (equal), Investigation (equal), Methodology (equal), Software (equal), Visualization (equal), Writing – original draft (equal), Writing – review & editing (equal)

Mark J Kushner 0000-0001-7437-8573
Conceptualization (supporting), Data curation (supporting), Methodology (equal), Software (equal), Supervision (equal), Writing – review & editing (equal)

Erik Wagenaars 0000-0002-5493-3434
Conceptualization (lead), Funding acquisition (lead), Project administration (lead), Resources (equal), Supervision (lead), Writing – review & editing (supporting)

Appendix A. Cross-sections

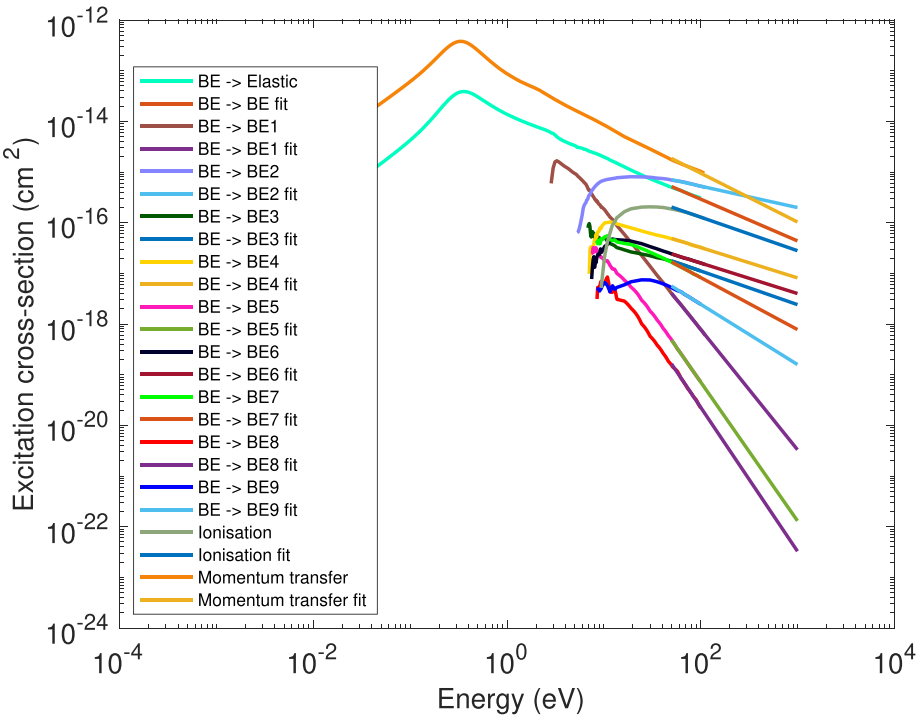

Figure A1. BE lumped state excitation cross-sections.

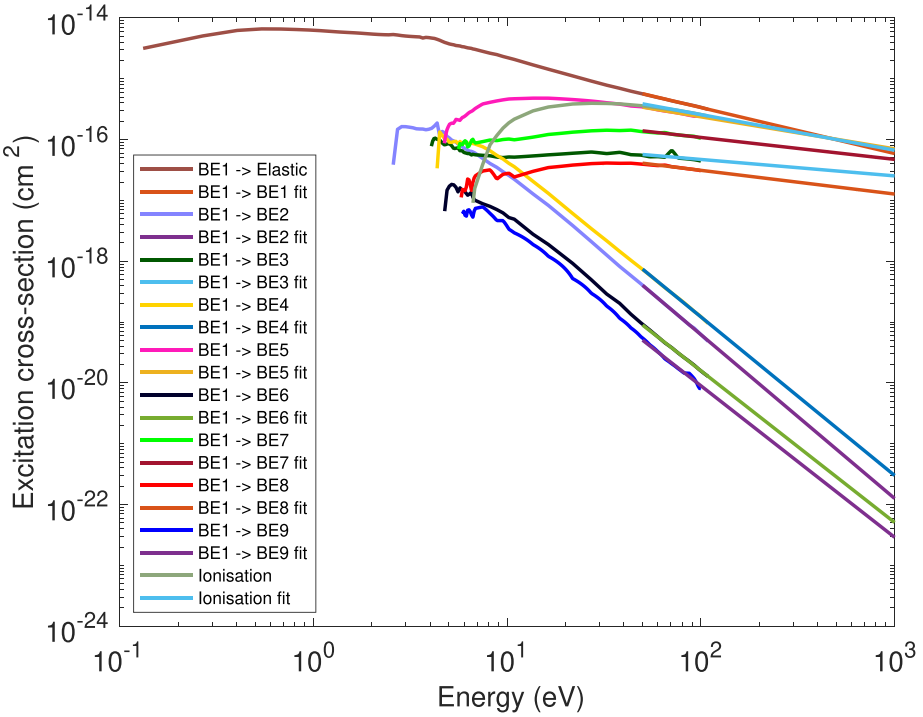

Figure A2. BE1 lumped state excitation cross-sections.

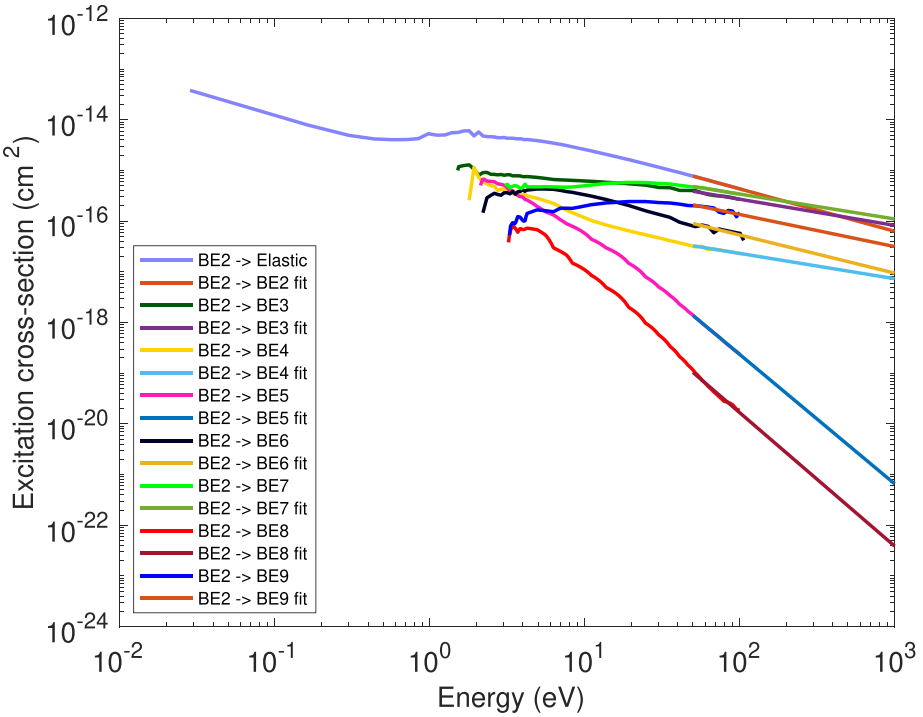

Figure A3. BE2 lumped state excitation cross-sections.

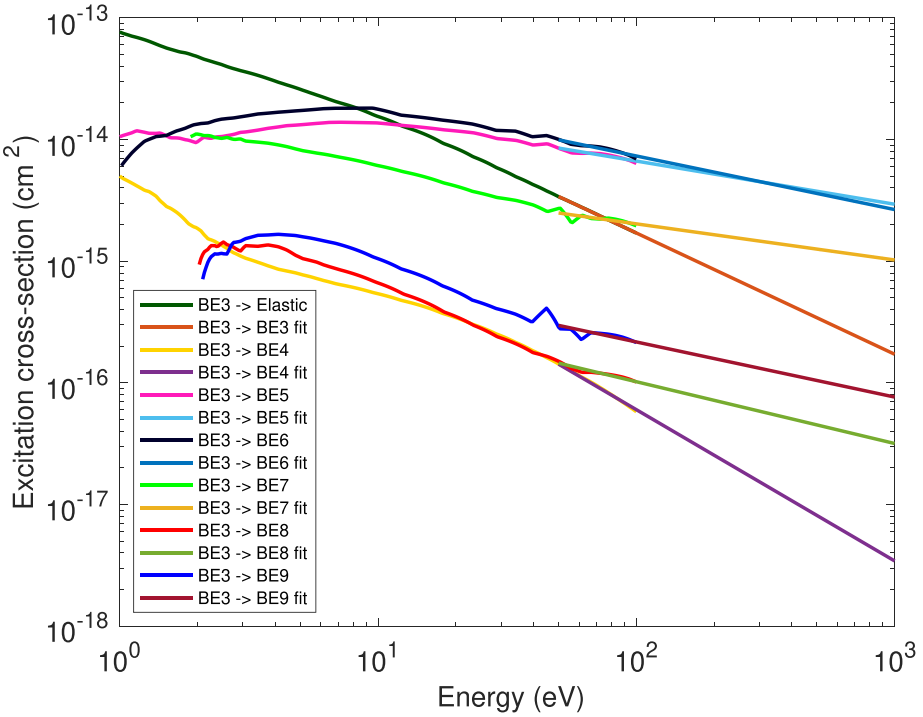

Figure A4. BE3 lumped state excitation cross-sections.

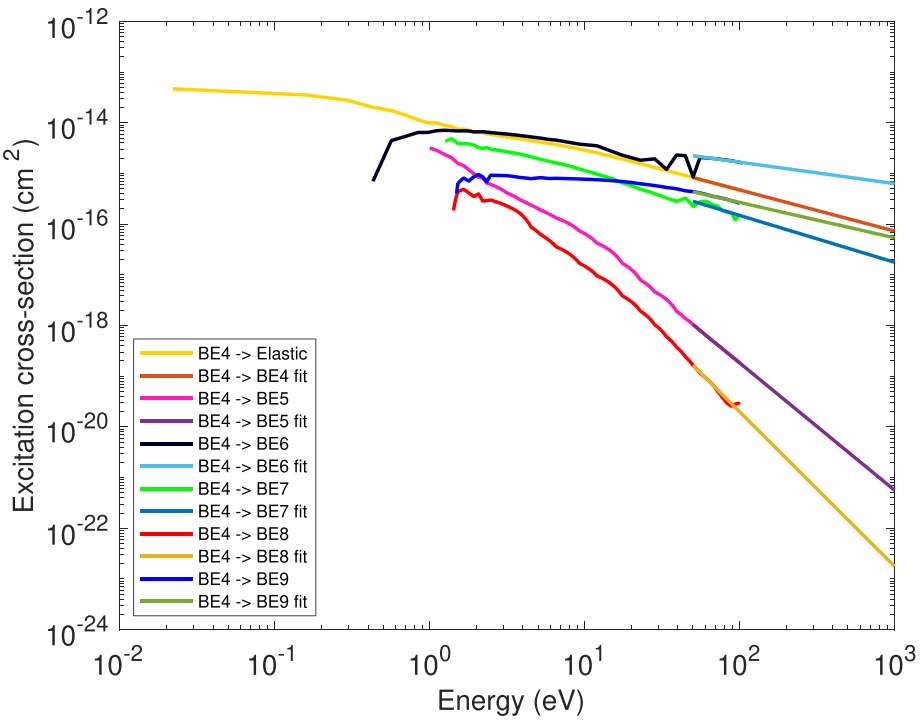

Figure A5. BE4 lumped state excitation cross-sections.

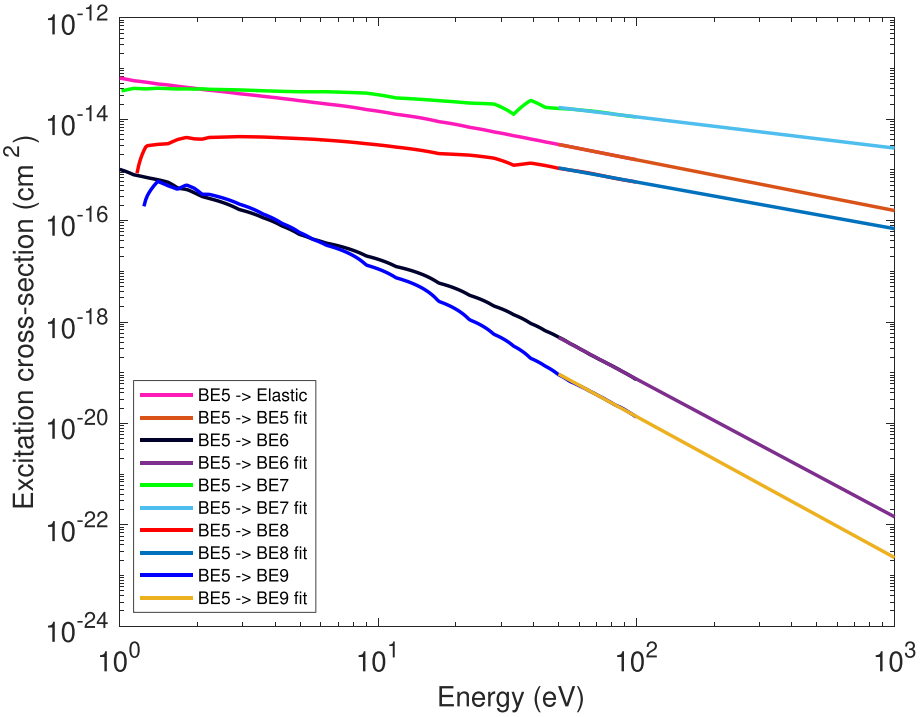

Figure A6. BE5 lumped state excitation cross-sections.

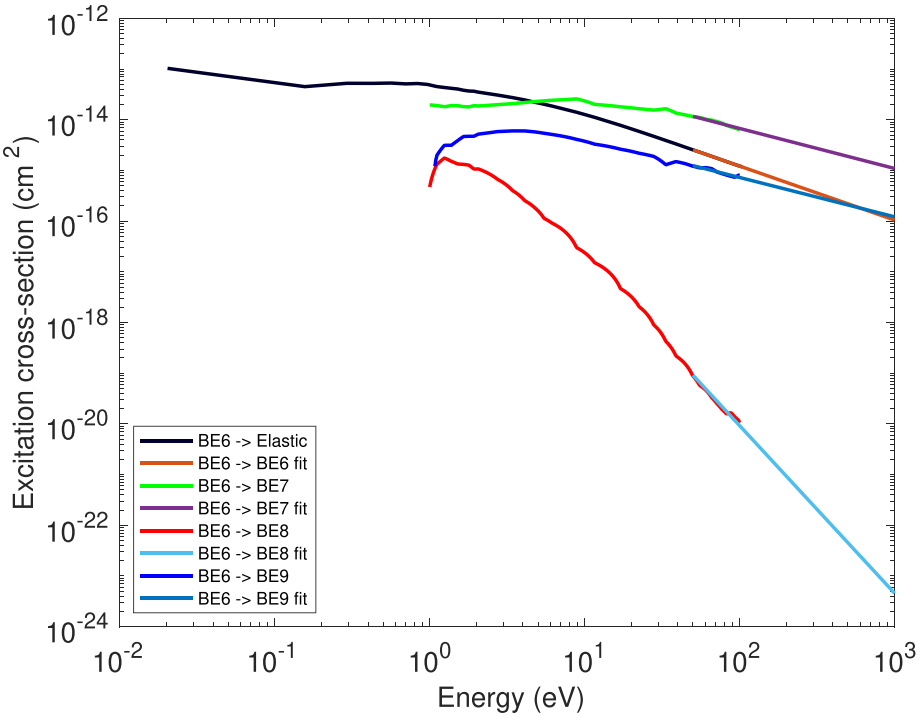

Figure A7. BE6 lumped state excitation cross-sections.

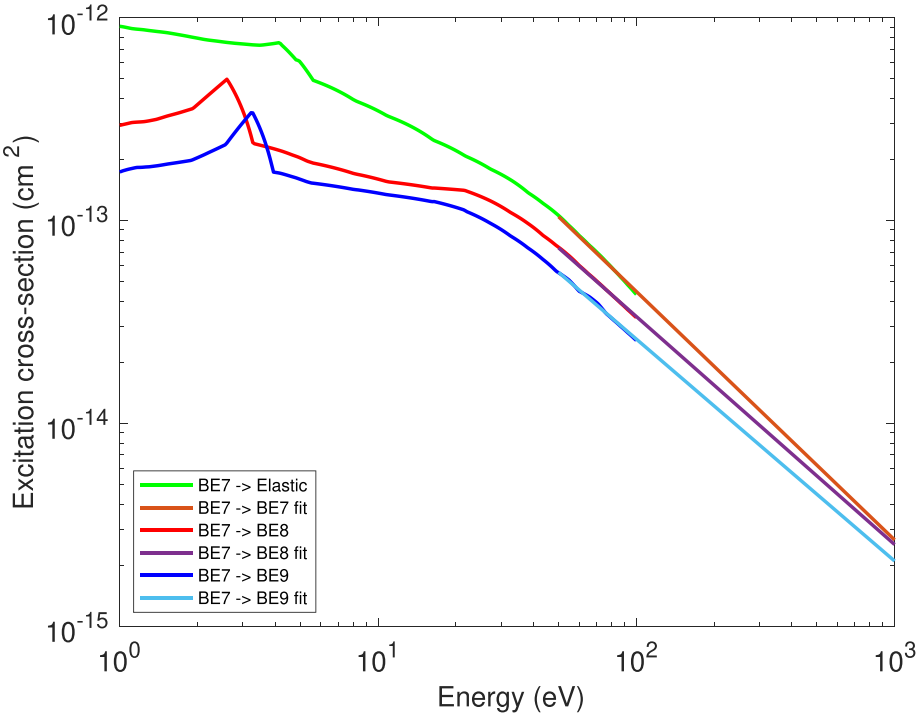

Figure A8. BE7 lumped state excitation cross-sections.

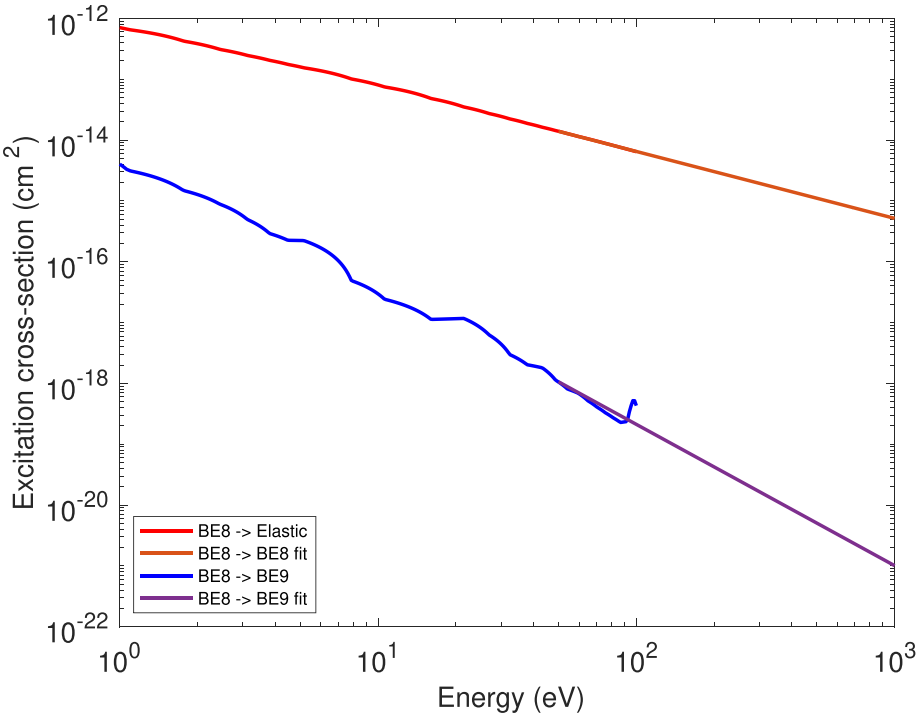

Figure A9. BE8 lumped state excitation cross-sections.

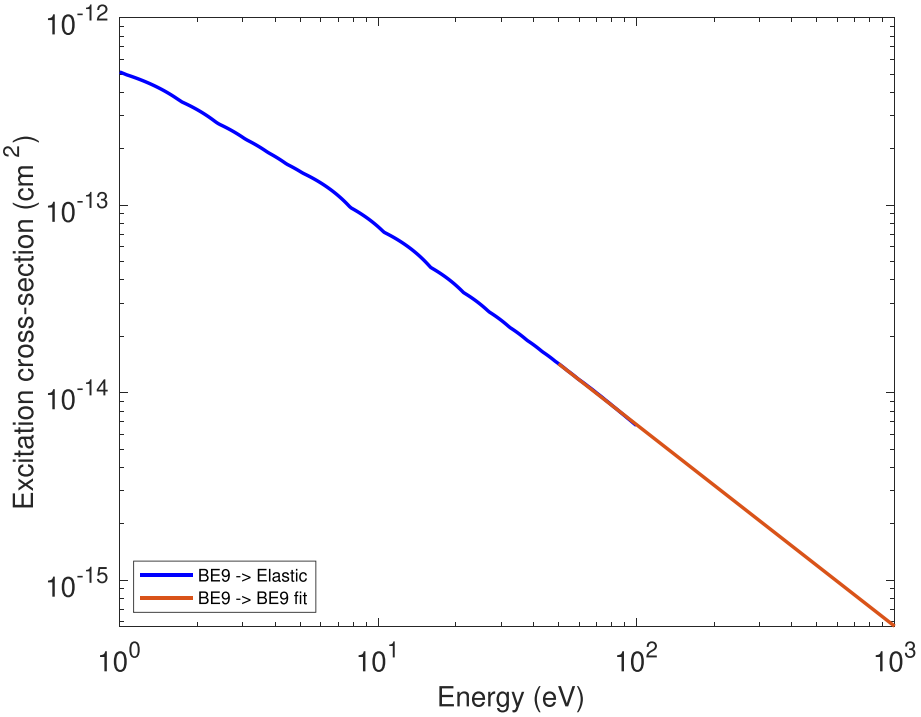

Figure A10. BE9 lumped state excitation cross-sections.

Appendix B. Sputtering yield

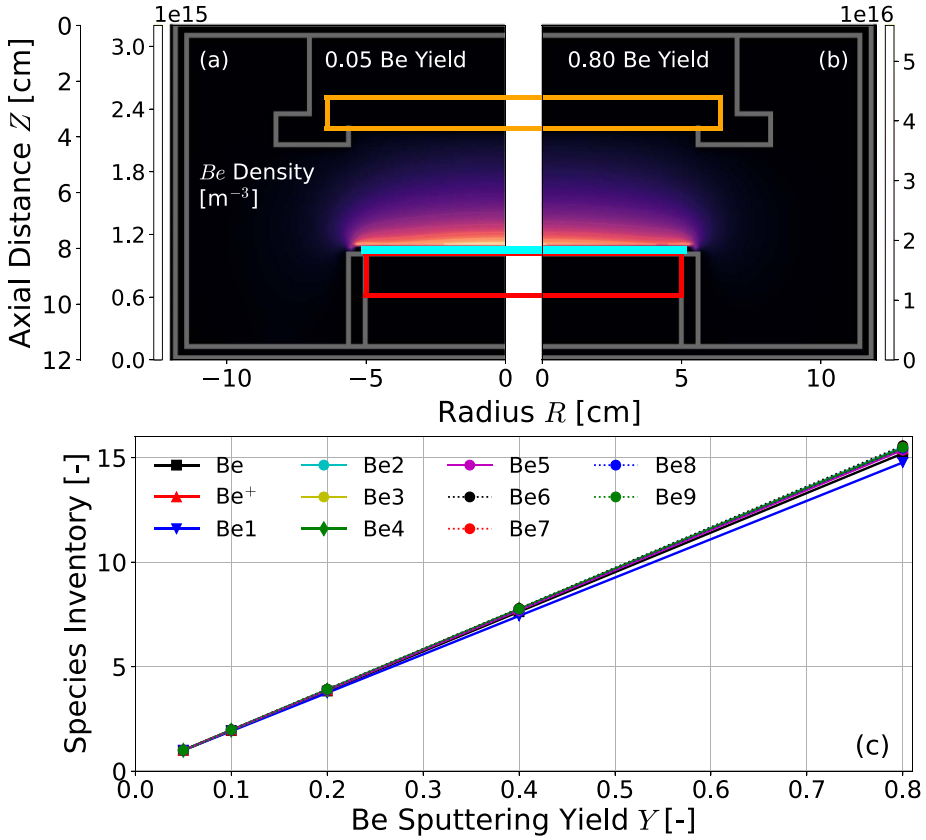

Figure B1. 2D Be ground state densities for (a) 0.00 probability and (b) 0.80 probability of Be sputtering in response to an incident cation. Sub-figure (c) shows 1D profiles of reactor integrated Be species densities for varying Be sputtering yields. Operating Conditions: Capacitive coupling employing 600 V_{pp}–1200 V_{pp} at 13.56 MHz, 10 mTorr argon. The scaling factor for the colour bar is noted at the top of each subfigure.

References

[1] Giancarli L M *et al* 2020 Overview of recent ITER TBM Program activities *Fusion Eng. Des.* **158** 111674
[2] Barabaschi P 2024 Press conference, new baseline to prioritize robust start to exploitation
[3] Brezinsek S *et al* 2011 Overview of experimental preparation for the ITER-like wall at JET *J. Nucl. Mater.* **415** S936
[4] Borodkina I *et al* 2024 Modeling of plasma facing component erosion, impurity migration, dust transport and melting processes at JET-ILW *Nucl. Fusion* **64** 106009
[5] Lederer G W, Foley N K, Jaskula B W and Ayuso R A 2016 Beryllium-A critical mineral commodity-resources, production, and supply chain. *Technical Report* 2016–3081 (U.S. Geological Survey)
[6] Ivanova D, Widdowson a, Likonen J, Marot L, Koivuranta S, Coad J P, Rubel M, Petersson P and Temmerman G D 2013 Assessment of cleaning methods for first mirrors tested in JET for ITER *J. Nucl. Mater.* **438** S1241
[7] Liptak A, Lawson K D and Hasan M I 1925 A molecular dynamics study of the sputtering processes of beryllium species by hydrogenic plasma *Sci. Rep.* **15** 15068
[8] Rubel M, Moon S, Petersson P, Widdowson A, Pitts R, Aleiferis S, Fortuna-Zaleśna E, Temmerman G D and Reichle R 2021 First mirror erosion-deposition studies in JET using an ITER-like mirror test assembly *Nucl. Fusion* **61** 046022
[9] Donné A *et al* 2007 Chapter 7: diagnostics *Nucl. Fusion* **47** S337
[10] Rubel M, Coad J P, Temmerman G D, Hakola a, Hole D, Likonen J, Uytdenhouwen I and Widdowson a 2010 First mirrors test in JET for ITER: an overview of optical performance and surface morphology *Nucl. Instrum. Methods Phys. Res. A* **623** 818
[11] Ivanova D, Rubel M, Widdowson a, Petersson P, Likonen J, Marot L, Alves E, Garcia-Carrasco a and Pintsuk G 2014 An overview of the comprehensive first mirror test in JET with ITER-like wall *Phys. Scr.* **T159** 014011
[12] Shaw D and Wagenaars E 2019 Modelling radio-frequency plasma cleaning of fusion optics *Plasma Phys. Control. Fusion* **61** 085031
[13] De Temmerman G *et al* 2021 Data on erosion and hydrogen fuel retention in beryllium plasma-facing materials *Nucl. Mater. Energy* **27** 100994
[14] Moon S, Petersson P, Rubel M, Fortuna-Zalesna E, Widdowson A, Jachmich S, Litnovsky A and Alves E 2019 First mirror test in JET for ITER: complete overview after three ilw campaigns *Nucl. Mater. Energy* **19** 59
[15] Brezinsek S 2015 Plasma-surface interaction in the be/w environment: conclusions drawn from the JET-ilw for ITER *J. Nucl. Mater.* **463** 11
[16] Patel B and Parsons W 2003 Operational beryllium handling experience at JET *Fusion Eng. Des.* **69** 689
[17] Marot L, Linsmeier C, Eren B, Moser L, Steiner R and Meyer E 2013 Can aluminium or magnesium be a surrogate for beryllium: a critical investigation of their chemistry *Fusion Eng. Des.* **88** 1718
[18] Razdobarin A *et al* 2015 Rf discharge for in situ mirror surface recovery in ITER *Nucl. Fusion* **55** 093022
[19] Berrington K A and Clark R E H 1992 Recommended data for electron impact excitation of Be+ and B+ ions *Nucl. Fusion* **3** 87 (available at: https://inis.iaea.org/records/fm5am-mey10)
[20] Bartschat K, Burke P and Scott M 1996 Electron impact excitation of beryllium *J. Phys. B: At. Mol. Opt. Phys.* **29** L769–72
[21] Ballance C, Griffin D, Colgan J, Loch S and Pindzola M 2003 Electron-impact excitation of beryllium and its ions *Phys. Rev. - At. Mol. Opt. Phys.* **68** 062705
[22] Clark R and Abdallah J 1996 Electron impact excitation cross sections for beryllium and boron *Phys. Scr.* **T62** 7
[23] Zatsarinny O, Bartschat K, Fursa D V and Bray I 2016 Calculations for electron-impact excitation and ionization of beryllium *J. Phys. B: At. Mol. Opt. Phys.* **49** 1
[24] Maihom T, Sukuba I, Janev R, Becker K, Märk T, Kaiser A, Limtrakul J, Urban J, Mach P and Probst M 2013 Electron impact ionization cross sections of beryllium and beryllium hydrides *Eur. Phys. J. D* **67** 2
[25] Huang S, Volynets V, Hamilton J R, Lee S, Song I-C, Lu S, Tennyson J and Kushner M J 2017 Insights to scaling remote plasma sources sustained in NF 3 mixtures *J. Vac. Sci. Technol. A* **35** 031302
[26] Huang S, Volynets V, Hamilton J R, Nam S K, Song I-C, Lu S, Tennyson J and Kushner M J 2018 Downstream etching of silicon nitride using continuous-wave and pulsed remote plasma sources sustained in Ar/NF3/o2 mixtures *J. Vac. Sci. Technol. A* **36** 021305
[27] Stafford D S and Kushner M J 2004 o2(1Δ) production in He/o2mixtures in flowing low pressure plasmas *J. Appl. Phys.* **96** 2451
[28] Lu J and Kushner M J 2000 Effect of sputter heating in ionized metal physical vapor deposition reactors *J. Appl. Phys.* **87** 7198
[29] Fuhr J R and Wiese W L 2010 tables of atomic transition probabilities for beryllium and boron *J. Phys. Chem. Ref. Data* **39** 1
[30] Gryziński M 1959 Classical theory of electronic and ionic inelastic collisions *Phys. Rev.* **115** 374
[31] Gryziński M 1965 Classical theory of atomic collisions. I. Theory of inelestic collisions *Phys. Rev.* **138** 336
[32] Gryziński M 1965 Two-particle collisions. II. Coulomb collisions in the laboratory system of coordinates *Phys. Rev.* **138** A322
[33] Gryziński M 1965 Two-particle collisions. I. General relations for collisions in the laboratory system *Phys. Rev.* **138** A305
[34] Bauer E and Bartky C D 1965 Calculation of inelastic electron-molecule collision cross sections by classical methods *J. Chem. Phys.* **43** 2466
[35] Moiseiwitsch B and Smith S 1968 Electron impact excitation of atoms *Rev. Mod. Phys.* **40** 238
[36] Manion J A *et al* NIST chemical kinetics database
[37] Quantemol.Quantemol DB (available at: https://quantemoldb.com/)
[38] Lieberman M A and Lichtenberg A J 2005 *Principles of Plasma Discharges and Materials Processing* (Wiley)
[39] Politzer P, Jin P and Murray J S 2002 Atomic polarizability, volume and ionization energy *J. Chem. Phys.* **117** 8197
[40] Hotop H and Niehaus a 1970 Reactions of excited atoms and molecules with atoms and molecules *Int. J. Mass Spectrom. Ion Phys.* **5** 415
[41] Temelkov K A, Vuchkov N K, Ekov R P and Sabotinov N V 2008 Determination of characteristic constants for some basic processes in plasma-diffusion, Penning ionization, asymmetric charge transfer *J. Phys. D: Appl. Phys.* **41** 105203
[42] Kushner M J 2009 Hybrid modelling of low temperature plasmas for fundamental investigations and equipment design *J. Phys. D: Appl. Phys.* **42** 194013
[43] Kushner M J 2003 Modeling of magnetically enhanced capacitively coupled plasma sources: ar discharges *J. Appl. Phys.* **94** 1436
[44] Lu J and Kushner M J 2001 Trench filling by ionized metal physical vapor deposition *J. Vac. Sci. Technol. A* **19** 2652
[45] Kinder R L and Kushner M J 2001 Wave propagation and power deposition in magnetically enhanced inductively coupled and helicon plasma sources *J. Vac. Sci. Technol. A* **19** 76
[46] Godyak V A and Piejak R B 1990 Abnormally low electron energy and heating-mode transition in a low-pressure argon rf discharge at 13.56 MHz *Phys. Rev. Lett.* **65** 996

[47] Kaganovich I D, Demidov V I, Adams S F and Raitses Y 2009 Non-local collisionless and collisional electron transport in low-temperature plasma *Plasma Phys. Control. Fusion* **51** 124003
[48] Weng Y and Kushner M J 1990 Method for including electron-electron collisions in Monte Carlo simulations of electron swarms in partially ionized gases *Phys. Rev. A* **42** 6192
[49] Stamp M, Krieger K and Brezinsek S 2011 Measurements of beryllium sputtering yields at JET *J. Nucl. Mater.* **415** S170
[50] Safi E, Björkas C, Lasa A, Nordlund K, Sukuba I and Probst M 2015 Atomistic simulations of the effect of reactor-relevant parameters on be sputtering *J. Nucl. Mater.* **463** 805
[51] Soni K, Moser L, Porosnicu C, Antunes R, Arredondo R, Dinca P, Steiner R, Marot L and Meyer E 2022 Deuterium plasma sputtering of mixed be-w layers *J. Nucl. Mater.* **564** 153671